Department of Physics and Astronomy

University of Heidelberg

Master thesis

in Physics

submitted by

Natascha Margarita Rupp

born in Herbolzheim

2015

On the detection of ^{222}Rn with miniaturized proportional counters: background, sensitivity studies and results for XENON1T

This Master thesis has been carried out by Natascha Rupp

at the

Max-Planck-Institut für Kernphysik

under the supervision of

Prof. Dr. Manfred Lindner

Zusammenfassung

Das radioaktive Isotop ^{222}Rn stellt eine der bedeutendsten intrinsischen Untergrundquellen in vielen Experimenten dar, die eine niedrige Ereignissrate erwarten. Das Edelgas emaniert permanent von fast allen Detektormaterialen und kann durch seinen Zerfall bzw. die Zerfälle seiner Töchterisotope das gesuchte Signal imitieren. Den Rahmen dieser Arbeit bildet das Experiment XENON1T, das sich mit Hilfe eines flüssig Xenon-Detektors den direkten Nachweis von massiven, schwach wechselwirkenden Teilchen (engl. "WIMPs") zum Ziel setzt. Diese stellen einen führenden Kanditaten für dunkle Materie im Universum dar. Eine aufwendige Messkampagne wurde durchgeführt, um die einzelnen Detektorbestandteile, die sich in Kontakt mit dem flüssigem Xenon befinden werden, auf ihre ^{222}Rn Emanationrate hin zu untersuchen. Die einzelnen Ergebnisse sowie eine Abschätzung der Gesamtemanationsrate werden erstmals präsentiert. Um die Detektion von ^{222}Rn mit Zählrohren weiter zu verbessern, wurden zudem die zwei Zählgase, $ArCH_4$ und $XeCH_4$, auf ihre Nachweisempfindlichkeit hin untersucht im Zusammenhang mit unterschiedlichen Untergrundabschirmungen. Für einen direkten Vergleich dieser Nachweisempfindlichkeit ist eine Energiekalibrierung notwendig, die im Zuge dieser Arbeit für $ArCH_4$ verbessert wurde.

Abstract

The radioactive isotope ^{222}Rn is one of the most crucial intrinsic background sources for experiments dealing with a low event rate. Being a noble gas, it permanently emanates from almost all materials that are used in the detector. Its decay or the successive decays of its daughter isotopes can mimic the searched-for signal. This thesis was carried out in the context of the experiment XENON1T which aims at directly detecting weakly interacting massive particles (WIMPs), that could be a candidate for the postulated dark matter in the Universe. An extensive measurement campaign was performed in order to determine the ^{222}Rn emanation rate of the detector components that will be in contact with the liquid xenon target. The individual results and an estimation of the detector's overall emanation rate are reported in this work for the first time. For a further improvement of the detection of ^{222}Rn with proportional counters, the sensitivity of the two counting gases $ArCH_4$ and $XeCH_4$ was studied in connection with different background shieldings. A direct comparison of the two counting gases makes an energy calibration necessary, the one for $ArCH_4$ was improved in the context of this work.

Contents

Introduction

Many observations of cosmological phenomena were done in the last decades that could not be explained by the existence of visible matter only. They formed the concept of a so far unknown kind of matter that does not interact with electromagnetic radiation and is thus left unseen. This so-called *dark matter* is searched by the direct detection experiment XENON1T that forms the framework of this thesis. In the first chapter a short summary of dark matter and the XENON1T experiment is given without striving for completeness. The focus of this work is placed on a crucial background source complicating the detection of the sought WIMP particles. Its originating from the decay of ^{222}Rn. The first part of this thesis is dedicated to this background source in XENON1T. We will describe the general procedure of ^{222}Rn emanation measurements. Furthermore we give the results of the ^{222}Rn emanation rates measured for the detector components that will be in contact with the liquid xenon that forms the target material of XENON1T. An overall emanation rate is estimated that presents an important input for the data analysis in the background discrimination. The knowledge we gained in the screening campaign is also meaningful in terms of a further background reduction for the future project XENONnT.

Striving for the detection of a new particle with the large and highly sensitive detector of XENON1T, we have to understand and improve every link in the chain that could lead to this detection. In terms of a better ^{222}Rn background determination, we have to start with the optimization of the emanation measurements based on the detection of ^{222}Rn decays. This detection is done with a rather small but also highly sensitive detector: a miniaturized proportional counter. In the second part of this thesis we will study the performance of two counting gases, $ArCH_4$ and $XeCH_4$, regarding their sensitivity in ^{222}Rn detection. We will identify the energy threshold that provides the highest sensitivity. This was studied in connection with background measurements for three different shielding options, either above ground or in an underground laboratory at Gran Sasso in Italy.

Chapter 1

Seeking the dark with XENON1T

One of the most astounding revelations of the last century in our understanding of the Universe is that the known, ordinary matter, made up of protons and neutrons accounts only for a small fraction of the matter in the Universe. The major ingredients, the *dark energy* and *dark matter* are still some of the greatest unsolved mysteries in cosmology at the present time. A promising description of dark matter could be provided by a postulated Weakly Interacting Massive Particle, the WIMP. The XENON1T experiment dedicates itself to the direct detection of this particle.

1.1 The quest for dark matter

The idea of a large non-luminous but massive amount of matter in our universe was introduced by Fritz Zwicky in the 1930's to explain the velocity dispersion of the galaxies in the Coma Cluster [57]. The galaxies are moving much faster than expected. Another famous hint for dark matter was discovered by Vera C. Rubin who studied the rotation velocities of stars in galaxies. In contradiction to the expected $v \sim 1/\sqrt{r}$ Keplarian decline of the velocities at large distances from the galaxy's center, the velocity is approximately constant [41]. An uniformly-distributed halo of dark matter could explain both mentioned phenomena. The content of dark matter in the Universe can be deduced by measurements of the cosmic microwave background (CBM) temperature anisotropies as they were most recently performed by the Planck satellite [38]. Calculations show that the energy in the Universe is made up of 4.9 % baryonic matter, 26.8 % dark matter and 68.3 % dark energy.

Dark matter could be described by a particle. Different candidates were suggested that need to fulfill certain properties. In order to be still present in the Universe the dark matter particles need to be stable or have a long lifetime compared to the age of the Universe. To account for the observed deflection of light rays by a gravitational field (gravitational lensing) that is greater than expected from the luminos mass only, dark matter particles need to interact gravitationally. Moreover they are not affected by the electromagnetic and strong force. In order to explain the structure formation in our Universe dark matter needs to be cold i.e. non-relativistic. This is one argument that rules out the relativistically moving neutrinos that are generally a good dark matter candidate within the known Standard Model of Particle Physics [18].

Models beyond the Standard Model suggest the existence of new particles which could account for the dark matter. One of them is called Weakly Interacting Massive Particle (WIMPs). Possible WIMP candidates are the lightest particle in the Kaluza-Klein theory [26] or the lightest neutralino in SUSY models [28]. An important argument for WIMPs is that the predicted relic dark matter density, fixed by the freeze-out in the early universe, is of the same order of magnitude as the observed density, if one assumes weak-scale interactions and a WIMP mass around the electroweak scale (GeV-TeV scale).

In general there are three approaches of detecting a dark matter particle. One of them is the their production in accelerators as it is done at the Large Hadron Collider (LHC) at Cern [23][12].The dark matter particles cannot be observed directly but rather through a missing energy signal.The second approach is the indirect detection. In cosmic regions with a high amount of dark matter, like galaxies, the self-annihilation of WIMPs or their decay into Standard Model particles could produce a measurable flux [34]. Experiments like IceCube [1], PAMELA [13] and the Fermi Gamma-Ray Space Telescope [11] search for these signatures. The third approach is referred as direct detection of a scattering process of a WIMP and target material. This method is used in XENON1T experiment which is looking for WIMP interactions via nuclear recoils in a liquid xenon target.

Assuming that the WIMP dark matter particles are penetrating the Earth with a certain flux it needs to be in principle possible to detected those heavy, neutral particles with an Earth based detector. The dark matter particles could depose their energy indirectly, via recoiling nuclei. The differential event rate of such

interactions can be written as [16]

$$\frac{\mathrm{dR}}{\mathrm{dE_R}} = \frac{\rho_\chi}{\mathrm{m_\chi m_N}} \int_{\mathrm{v_{min}}}^{\mathrm{v_{esc}}} \mathrm{v\ f(v)}\ \frac{\mathrm{d}\sigma_{\mathrm{WN}}}{\mathrm{dE_r}}\ (\mathrm{v}, \mathrm{E_R})\ \mathrm{dv}. \tag{1.1.1}$$

Thereby describes f(v) the dark matter velocity distribution in the galactic region close to our solar system. The escape velocity v_{esc} is measured [48] and $\mathrm{v_{min}}$ is the minimal velocity needed for a recoil of energy $\mathrm{E_R}$ in the case of maximum energy transfer by 180° backscattering. The local dark matter density ρ_χ is assumed to be $\sim 0.3\,\mathrm{GeV}$ by recent results [54]. The WIMP and target nucleus masses are denoted by m_χ and m_N, respectively. The differential cross section of a WIMP-nucleus scattering $\frac{d\sigma_{WN}}{dE_r}$ splits up in a spin-dependent and spin-independent part. The spin-dependent part scales with the J(J+1), whereby J is the nuclear spin and the spin-independent part scales with A^2 and A is the atomic number [16].The overall shape of the spectrum will be exponentially decreasing with increasing recoil energy in the case of spin-independent interactions. This requires detectors with a low energy threshold to exploit as much as possible from the expected recoil spectrum. The total event rate scales with A^2 which favors heavy nuclei like xenon as target material.

If the observed rate is significantly higher than the expected background rate a signal can be claimed whereas an equal rate of signal and background derives further exclusion limits. Current limits on the spin-independent WIMP-nucleon cross section are shown in Fig. 1.1 for various dark matter experiments. The LUX experiment, that uses liquid xenon as target material, sets currently the most stringent spin-independent WIMP-nucleon cross section with an upper limit of $7.6 \cdot 10^{-46}\,\mathrm{cm}^2$ at a WIMP mass of $33\,\mathrm{GeV/c}^2$ [3]. The SuperCDMS experiment uses germanium crystals to derive the recoil energy by measuring ionization and phonon energy. It sets the most stringent limit on cross sections for low WIMP masses [2]. We focus on the XENON1T [10] experiment in the following. The experiment XENON100 [7] did not find any evidence for dark matter but with 35 times more target mass and a background goal 100 times lower, XENON1T sensitivity to spin-independent WIMP - nucleon cross sections is expected to be $2 \cdot 10^{-47}\,\mathrm{cm}^2$ at a WIMP mass around $40\,\mathrm{GeV/c}^2$. The planned upgrade XENONnT will further improve the sensitivity as indicated in Fig.1.1.

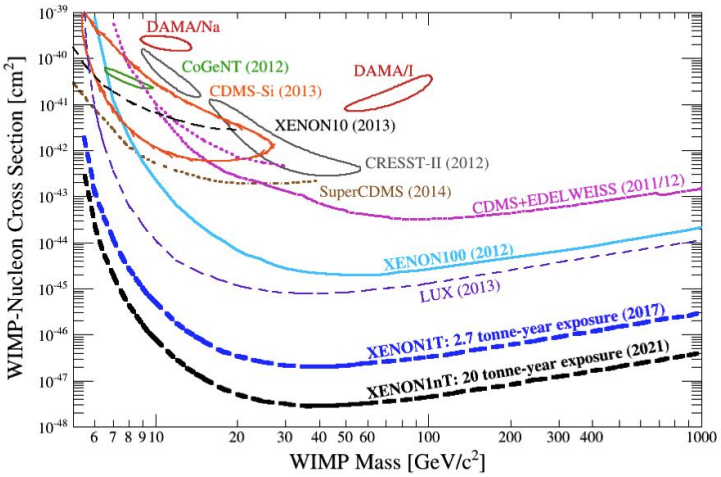

Figure 1.1: WIMP-nucleon scattering cross section with the WIMP mass as free parameter for various experiments. The expected sensitivities of the XENON1T experiment and its upgrade, XENONnT are shown that will further improve the currently best limit on the cross section measured by the LUX experiment [60].

1.2 The XENON1T dark matter experiment

The XENON1T experiment is named after the element that is used as target material. Xenon offers several advantages that make its preferential in the WIMP search. Its ionization and scintillation properties enables the detection of WIMPs and their discrimination from background. The high atomic number enhances the cross section for spin-independent interactions. Xenon has a high stopping power which provides a good self-shielding capacity for background reduction. In the subsequent section the XENON1T detection principle is explained followed by an overview of the detector set-up.

1.2.1 XENON1T detection principle

The XENON1T detector is placed in the underground "Laboratori Nazionale del Gran Sasso" (LNGS)[1] in Italy to shield it from cosmic radiation. It innermost part consists of a two-phase liquid-xenon time projection chamber (TPC) that can be seen as a sketch in Fig. 1.2. It will contain 3.3 tons liquid xenon with a gaseous xenon phase on the top. An incident particle can be distinguished by its interaction with the xenon atoms. A γ-ray or an electron interacts mostly with the orbital electrons and produces an electronic recoil. A heavy, neutral

[1] https://www.lngs.infn.it

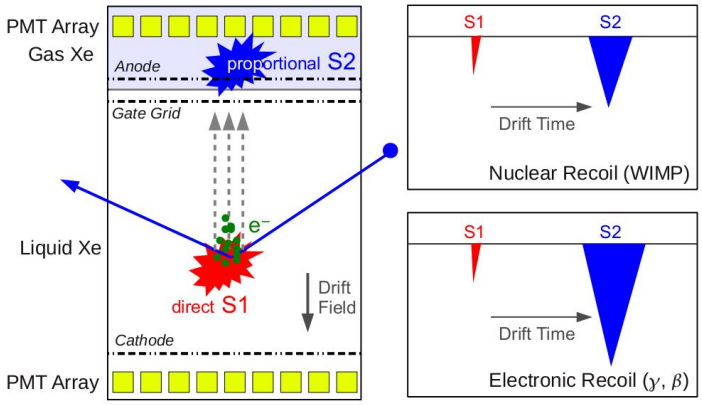

Figure 1.2: Left side: Detection principle of a two-phase time projection chamber (TPC). Interactions in the liquid xenon volume (LXe) create both prompt scintillation light (S1) and ionization electrons. In the applied electrical field the electrons are drifted to the liquid-gas interface. Extracted into the gaseous xenon (GXe) they generate secondary scintillation signal (S2). Right side: Signal characteristic due to electronic or nuclear recoil of xenon atoms. The ratio of S1/S2 is used for background discrimination [60].

particle like a neutron or the WIMP scatters off elastically from the xenon nucleus that in turn scatters off the surrounding xenon atoms. This is referred as nuclear recoil. In both scenarios, electronic and nuclear recoil, excitation and ionization of the xenon atoms occur. In the process of disexcitation photons are produced that could be detected by ~ 250 photomultiplier tubes (PMT) installed at the top and bottom of the TPC. This direct scintillation light is also called prompt signal or S1. The ionization electrons are drifted from the interaction site to the gaseous phase by an applied electric field. By reaching the liquid-gas interface they get extracted and further accelerated by a stronger field. In the gas phase they interact with the xenon atoms, producing a number of scintillation photons which is proportional to the number of ionization electrons. This proportional scintillation light is again detected by several PMTs. This delayed signal is also called S2 signal. As indicated in Fig. 1.2 the ratio of the S2 and S1 signals depends on the type of recoil and can be used for the discrimination of incident particles. The time difference between the S1 and S2 can be translated by the constant drift velocity of electrons in the homogeneous drift field into the z-position of the interaction vertex inside the TPC. The hit pattern of the S2 signal allows a reconstruction of the (x,y)-position. The knowledge of the spatial position of an event provides an important tool to identify background events.

The detector is placed in a 9.6 diameter water tank to protect it from ambient radiation. The tank will also provides a muon veto since it will be equipped with PMT detecting Cherenkov light induced by muons crossing the water. The muon flux is already reduced by a factor of 10^6 as the detector is installed in a depth of 3800 m.w.e [22]. One of the most dangerous intrinsic background inside the liquid xenon like the radioactive decay of ^{85}Kr which is always contained in commercial xenon. The other crucial intrinsic background source is ^{222}Rn, that permanently emanates from all detector materials. The first part of this thesis deals with the recent ^{222}Rn emanation measurements that are done before the detector parts were assembled. In the upcoming section 1.2.2 the detector set-up is described in more detail since most of the detector parts that will be in contact with the target material were investigate on their ^{222}Rn emanation rate.

1.2.2 Detector set-up

Fig. 1.4 shows an excerpt of the the XENON1T gas system, that will be explained in the following, as most of its components were investigated in order to determine their ^{222}Rn contamination. The exact method of measuring it will be explained in the next chapter 2.

We start from the core of the detector made up of the cryostat, also called inner vessel. It will contain the ~ 3 tons of liquid xenon, the TPC and the PMTs. The TPC is encased in PTFE (Polytetrafluoroethylene), as this material provides a high reflection probability of UV light and accordingly scintillation light triggered by a hypothetical WIMP interaction. The inner vessel is surrounded by the outer vessel, that serves as vacuum vessel. It should thermally decouple the inner vessel from ambient temperature to keep the the liquid xenon at a temperature of 180 K. From the cryostat the xenon could be transferred to three main parts of the gas system: the cryogenic system, the purification system and to the recuperation and storage system (ReStox). The transport is performed through a pipe system. The pipes that are connected to the inner and outer vessel are shown in Fig.1.3. The prefix number stands for the respective diameter of the pipe in the following description. The top of the outer vessel is connected to the 400 mm pipe that carries the isolation vacuum. It is colored in blue in Fig.1.3. The top of the inner vessel is connected to the 250 mm pipe, indicated in green, that is surrounded by the 400 mm pipe. Hence their volumes are completely separated. Inside the 250 mm pipe is the red indicated 100 mm pipe and several thinner pipes. All of them are open towards the inner vessel . The xenon is mainly liquid in the

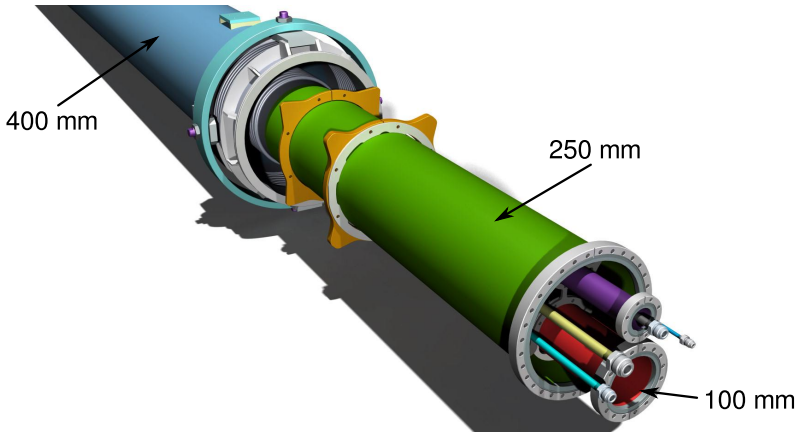

Figure 1.3: Pipes that connect the inner and outer vessel of the XENON1T detector with gas system. The blue indicated 400 mm pipe carries the isolation vacuum, the green indicated 250 mm pipe is used to transfer gaseous xenon to the cryogenic system. Red colored is the 100 mm pipe containing the cable for the PMT support. The thinner pipes are connected with other parts of the gas system or serves for calibration source access [60].

cryostat with a gaseous phase on its top. For cooling, the gaseous xenon it is transferred through the 250 mm pipe to the cryogenic system, marked in a blue box in Fig.1.4. It contains Pulse Tube Refrigerator (PTR) that provide a high cooling power to achieve liquid xenon temperature. They are mounted on a copper block and the cooling power is delivered to the xenon system through a cold finger. The gaseous xenon is cooled and liquefied at this cold finger, collected by dropping into a funnel and flows back to the cryostat. The xenon can also be transferred from the cryostat to the purification system, which is not shown on Fig.1.4 but the pipes leading to it are indicated. The purification system includes two getters and two QDrive pumps. A getter is used to purify xenon from electro-negative impurities that could reduce the electron drift length. The xenon can only be purified by the getters in the gaseous state but needs to be liquid inside the TPC. Heat exchangers will be used to evaporate liquid xenon and recondense xenon gas. One of them is indicated in red. The 100 mm pipe is marked in green in Fig.1.4. It contains cables for the PMT supply[2]. A further vessel is mounted at an external port of the 100 mm pipe and serves as feedthrough for the included cables. If an emergency occurs, the xenon can be stored in another pressure vessel, ReStox, made with a built-in high-power cooling system.

[2]The cables consist of about 4.5 km of Kapton single wire cables for the PMT HV supply, $\sim$ 4 km of Teflon coax cable for the PMT signal read out, $\sim$ 37 m of optical fiber used for the PMT calibration and about 100 m of Kapton cables for the grids in the TPC that provide the drift field.

Its not drawn in Fig.1.4 but the connecting pipes are shown. Moreover there is another thin pipe for calibration sources access.

The ^{222}Rn contamination of all described parts, that are permanently in contact with xenon were measured, either individually or combined with other parts. ReStox was not investigated as it is not included in the xenon recirculation loop during normal operation. The ^{222}Rn originating from the recovery vessel is no constant contribution and decays within a few days after filling the xenon to the detector. The information of this section 1.2.2 were taken from [5] and [6] and the interested reader is referred to these documents for more information.

In the next chapter 2 we will start with the description of ^{222}Rn as background source in XENON1T. We will give an overview on the measurement procedure in order to determine the ^{222}Rn emanation rate of the XENON1T detector parts that will be in contact with the target material. In the last part of this chapter we present the results of the ^{222}Rn emanation measurements that were completed by the time of writing as well as an estimation of the overall ^{222}Rn emanation rate in XENON1T.

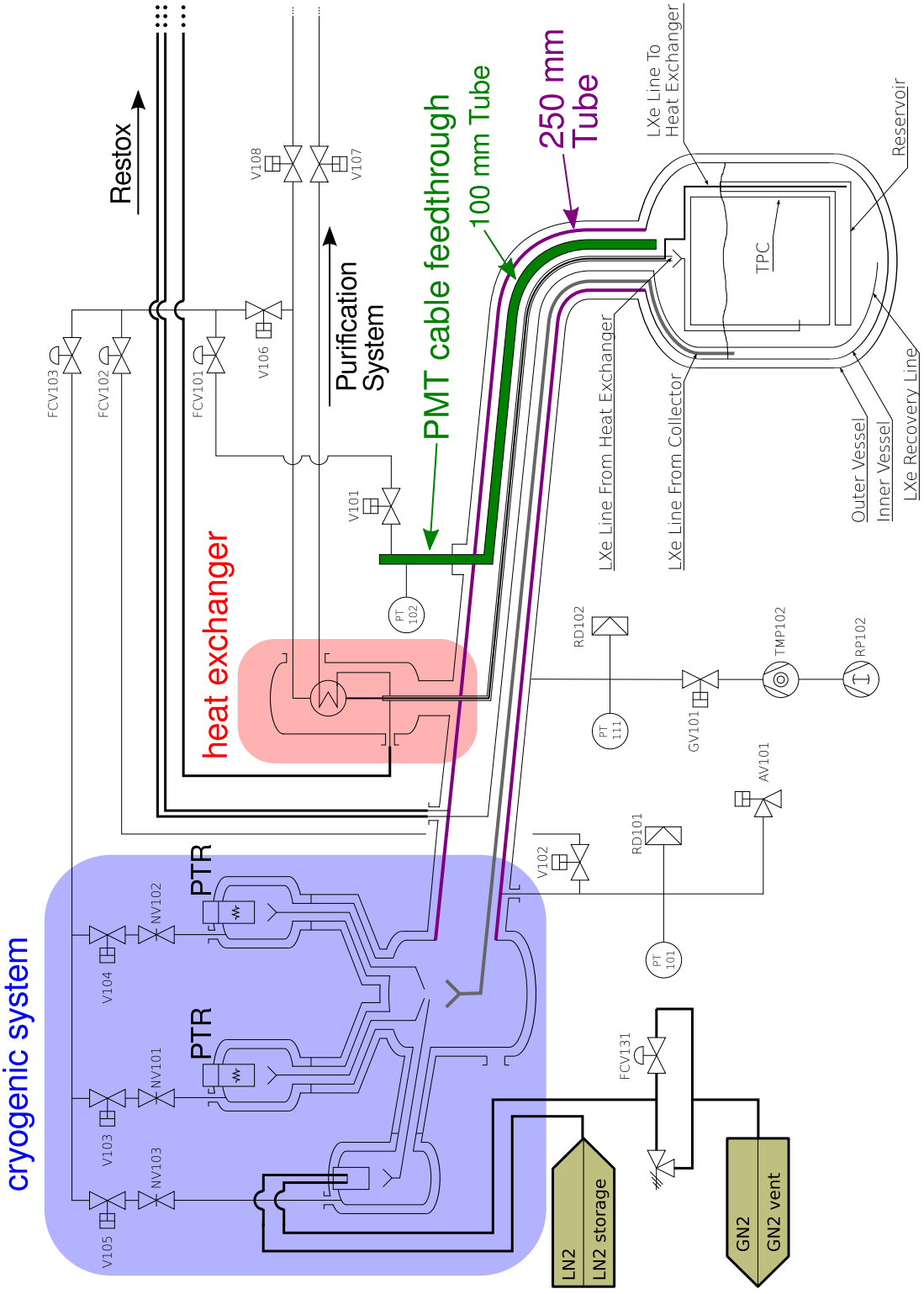

Figure 1.4: Excerpt of the the XENON1T gas system [60].

Chapter 2

On the radon background in XENON1T

Radon belongs to the most threatening intrinsic background sources in many experiments searching for rare interaction rates. This is especially the case for experiments like XENON1T, that are using liquid noble elements as target material. Radon has similar chemical properties which makes an effective separation difficult. In section 2.1 we will describe radon as background source in more detail. One approach to keep the radon contribution to the overall background rate as low as possible is a careful selection of detector materials with a low radon emanation rate. This strategy was also applied for XENON1T resulting in an intensive measurement campaign including most of the detector components. The measurement procedure is explained in section 2.2. In section 2.3 the results are given as well as an estimation of the overall radon contribution to the background in XENON1T.

2.1 Radon as background source

The element radon (Rn) belongs to the class of noble gases among helium (He), neon (Ne), argon (Ar), krypton (Kr) and xenon (Xe) ordered by ascending mass whereby radon is the heaviest. It is the only noble gas without any stable isotope. Still abundant in nature are the ones that occur as intermediate step in the primordial decay chains of ^{235}U, ^{238}U and ^{232}Th. Out of these isotopes ^{222}Rn and ^{220}Rn have the longest half-lives with $T_{1/2}^{Rn222} = 3.82\,\text{days}$ and $T_{1/2}^{Rn220} = 55.6\,\text{s}$ [ISO]. Fig. 2.1 shows the decay chain of ^{238}U, which is most relevant in the following discussion. The chain includes ^{226}Ra, the mother nuclei of ^{222}Rn, that is existing in almost all materials. In the subsequent work the term radon always

stands for this particular isotope. Noble gases rarely participate in chemical reactions. This results in a comparable large diffusion length in any material. Hence ^{222}Rn can leave its point of creation and might have enough time to travel over large distances before disintegrating. Thereby it could also reach the sensitive volume of the detector. The decay of ^{222}Rn induces a series of subsequent decays accompanied by the emission of γ rays, α and β particles until the stable isotope of ^{206}Pb is attained (see again Fig. 2.1). These particles can interact with the target material. Depending on the searched signal characteristic some of them could mimic it by this interaction. This turns the permanently emanating radon to a serious background source for experiments dealing with a low event rate.
In XENON1T the signal of interest is induced by interaction of a hypothetical WIMP with a xenon atom leading to a nuclear recoil. The expected event rate for this interaction is the highest at rather low recoil energies in the range of a few tenths of keV. The energies of the α particles within the decay chain of ^{222}Rn are far too high that their interaction with the xenon atoms could be misidentified as a WIMP particle. More crucial are the β-decays. The continuous β-spectrum has an energy range from 0 keV up to the Q-value of the particular decay. This means that the β particles can also deposit low energies depending on the energy loss due to the not detected antineutrino. Four β-decaying isotopes occur in the ^{222}Rn decay chain: ^{214}Pb,^{214}Bi,^{210}Pb and ^{210}Bi. Amongst these isotopes, the decay of ^{214}Pb turns out to be most critical background contribution [19]. The β-decay of the isotope ^{214}Bi are followed immediately by the high energetic α-decay of ^{214}Po. Events showing this characteristic coincidence signature are rejected in more than 50 % of the time [19]. Since the isotope ^{210}Pb has a half-life of 22.6 years, much longer than the expected running time of XENON1T, its decay and all subsequent progenies, including ^{210}Bi are efficiently suppressed and thus insignificant. The goal for XENON1T will be to reach a ^{222}Rn contamination of 1 μBq/kg xenon, a reduction of a factor $\sim$50 with respect to the current values reached in XENON100 [36]. This results in am overall emanation rate of $\sim$ 3 mBq for the $\sim$ 3.3 tons of liquid xenon. Radon has the potential to become the most dominant intrinsic background in XENON1T as it is homogeneously distributed in the liquid xenon [8] and a fiducial volume cut might not be sufficient for its rejection. Events close to the wall of the TPC are most likely induced by radioactivity of the detector material. The fiducial volume cut discards these events [1]. One way to keep the ^{222}Rn contamination as low as possible

[1] Thereby also the short-lived ^{220}Rn is rejected that has not enough time to distribute all over the liquid xenon [52].

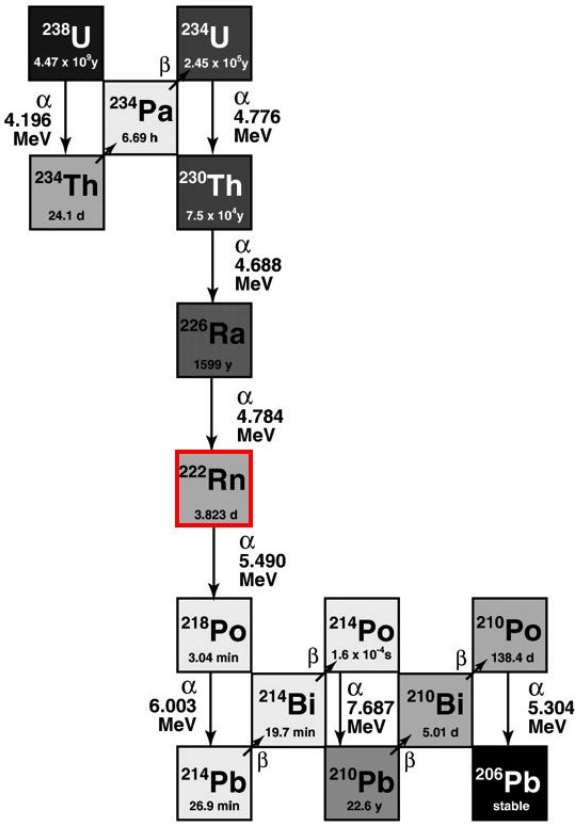

Figure 2.1: Decay chain of ^{238}U including ^{222}Rn and its daughter isotopes [63].

is a careful selection of radio-pure detector materials. The detector parts that are directly in contact with the liquid or gaseous xenon are thoroughly screened i.e. their ^{222}Rn saturation activity is measured. The mother nuclei ^{226}Ra has a half-life of $T_{1/2}^{Rn226} = 1600$ years. The constant decay rate of ^{226}Ra leads to a constant production rate of ^{222}Rn and hence to a constant emanation rate. After a few days the production and decay of ^{222}Rn is in nearly in equilibrium, because strictly speaking the saturation activity can never absolutely be reached and only approximated. Whenever the saturation activity is mentioned in the following, one should keep in mind that it is rather an approximated saturation activity. This is also considered in the data evaluation. Knowing the saturation activity is important for the data analysis of XENON1T. In addition it gives the possibility to find an alternative material if the screened one has a radon emanation rate higher than the experiment's requirements. In the next section the method of measuring the saturation activity is explained, followed by the current ^{222}Rn emanation results of XENON1T.

2.2 ^{222}Rn emanation measurements

Materials and parts of the detector whose ^{222}Rn emanation rates could contribute to the background of the experiment are thoroughly investigated. This investigation is based on the measurement of the particular ^{222}Rn emanation rates. The following section should give an overview of the individual steps of a ^{222}Rn emanation measurement. The measurement procedure splits up in several steps, that will be explained in more detail below:

- **preparation:** investigated sample is sealed it in a container and impurities are removed
- **extraction:** after a few days of radon emanation the ^{222}Rn atoms are extracted from the container
- **purification:** the emanated sample gets purified
- **counter filling:** the sample is filled in a proportional counter for the detection of ^{222}Rn decay
- **detection of ^{222}Rn decay and data evaluation:** the saturation activity is determined by the detected counts

To perform the first three steps we use a so-called emanation system whereas the purification and counter filling is done with a construction made out of glass, the so-called gasline. Important components in these two systems are several U-shaped traps. They are filled with adsorber materials. This material is used to store radon atoms and separate them from impurities that can also emanate from the investigated sample. The separation is realized by gas chromatography that in turn bases on the diverse adsorption properties of the gaseous components that should be separated. In order to flush the emanated sample through the system, helium is used as carrier gas. Also other inert gases like neon, argon or nitrogen can be used depending on the particular requirements of the measurement. To increase the effect of adsorption one uses adsorbents with a large surface like activated charcoal. In addition one can cool the adsorber material to increase its adsorption capacity. More details can be found in [19]. All the relevant devices that are involved in the measurement were screened and carefully selected to assure a low intrinsic background contribution (blank contribution).

Preparation

The emanation system at Heidelberg consists of two stainless steel emanation chambers with a volume of 20 l and 80 l, the so-called helium trap, the radon trap and a scroll pump. A simplified sketch of the system can be seen on Fig 2.2, showing only one container. The system is used for the sample's preparation as well as the subsequent collection of the emanated radon atoms (together with non-avoidable impurities).

We start with the description of the preparation. In this step superficial impurities like radon containing air should be removed. They would misleadingly increase the measured saturation activity or complicate the counter filling. At first the sample gets enclosed in one of the chambers which is afterwards evacuated. Helium, or any other carrier gas is flushed through it. It is important that no ambient radon is brought inside the chamber. Consequently it needs to be ensured that the helium itself is radon-free as radon is always contained in commercially available gases. For this purpose the helium trap is used. Since it could be in turn contaminated with radon it needs to be purified. This is the first step of every measurement and the preparation. The helium trap is baked while helium is streaming through it. The impurities desorb from the activated charcoal and are flushed away until the trap is considered to be radon-free. After this cleaning process the trap is cooled down with LN_2 to a temperature of $-196\,°C$. This turns the situation around. Now the cleaned charcoal itself serves for purification of the helium that is still streaming through by adsorbing the radon. The radon-free helium is flushed through the chamber and removes the mentioned impurities. In the last step the chamber is filled with the carrier gas to a slight overpressure to avoid air entering in case of a potential leak. At this stage no ambient radon should be left inside. The radon atoms that are extracted after some days should only originate from the sample and the blank contribution of the vessel. Note that if one waited several half-lives of ^{222}Rn the ambient radon, that could still be present after preparation, would be decayed. Only radon that constantly emanates from the sample would be present. However in practice one seldom has this time which makes a careful preparation necessary.

Extraction

The extraction procedure also begins with the described purification of the helium trap and the carrier gas. The radon trap is connected to the system and needs to

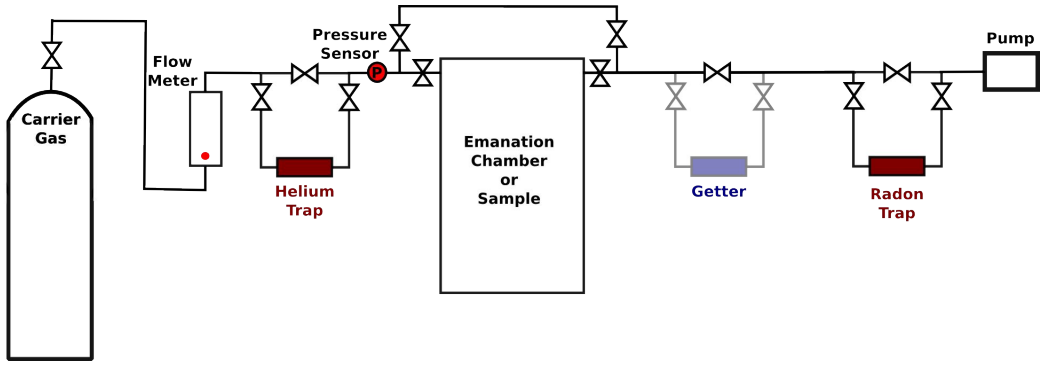

Figure 2.2: Emanation system used to prepare samples and collect the ^{222}Rn atoms that have emanated. The helium trap is used to purify helium whereas the radon trap is used to collect the emanated atoms. The getter can be optionally included for purification.

be cleaned from radon in the same manner as the helium trap. Once this is done the extraction can start. The charcoal inside the radon trap is cooled down with LN_2 whereby its adsorption capacity is increased. Radon-free helium is used to flush the gas slowly out of the chamber and through the radon trap. Thereby the radon atoms are adsorbed by the charcoal and hence stored. The low velocity should assure that the charcoal is not warmed up by the subsequent gas flow. Other impurities like organic outgassing of the sample can also be undesirably stored in the trap. In general the amount of impurities can be minimized with a non evaporable getter as it is already used in the gasline. This device has a metallic surface and operated in hot state it removes chemically reactive gases from sample [42]. It was shown in the course of emanation measurement for XENON1T that a getter installed in front of the radon trap's inlet reduces impurities during the extraction process.

Purification and counter filling

The gasline includes several traps with different kinds of adsorber materials. All of them need to be cleaned from impurities before they get in contact with the sample. This is done as described before in the case of the helium and radon trap. Afterwards the gaseous sample is flushed through a clean trap containing glass wool at a temperature of $\sim -30\,^{\circ}\mathrm{C}$. This temperature is obtained with ethanol that is cooled with LN_2. Water vapor and some organic components freeze out in this trap. The remaining sample is again adsorbed in a trap containing activated charcoal that is cooled with LN_2. This trap gets at first inserted into ethanol at $\sim -130\,^{\circ}\mathrm{C}$ while pumping at it. Thereby potentially adsorbed helium and other

gaseous components are removed. Afterwards the trap is baked and the radon atoms desorb together with remaining impurities. The gas mixture is connected with a hot getter that removes chemically reactive gases. The impurity-free radon sample is mixed with counting gas whose amount is determined by the maximum allowed pressure of $\sim 1\,\mathrm{bar}$ inside the active volume of the counter. Mercury is used to push the sample and the counting gas into the counter and seal it effectively.
Note that the step of saving the radon atoms in a trap after extraction is not mandatory but rather convenient in practice. This step can be omitted if the emanation chamber could be directly connected to the gasline. In practice this is only done for small samples that can be stored in smaller and more handy vessels. The storage in a trap is necessary for extraction performed on another place as the counter filling. An example is the measurement of the cryostat of XENON1T. It was prepared and extracted at the construction hall of the company that fabricated it but the sample was filled in a proportional counter at our gasline permanently installed at LNGS. This case shows that a sample itself can serve as its own emanation chamber if it can be sealed from the outside and if we are only interested in the emanation rate of its inner surface.

Detection of ^{222}Rn decay

The quantification of the ^{222}Rn atoms is done with a miniaturized proportional counters. One example is shown in Fig. 2.3. They were originally developed for the solar neutrino experiment GALLEX at MPIK (Max Plank Insitut für Kernphysik) in Heidelberg, Germany. The counter has a cylindrical housing made out of low-radioactive synthetic quartz glass that contains the likewise cylindrical cathode made out of iron or silicon. A thin and taut tungsten wire along the z-axis serves as anode. The volume of the counter is roughly $1\,\mathrm{cm}^3$. It differs slightly among different counters since they are hand-made in the glass blowing workshop at MPIK. Different counting gases are used. In the standard procedure it is either a mixture of 90 % argon and 10 % methane (P10) or $XeCH_4$ with the same ratio of noble gas and methane. The calibration of the counters is done with a ^{55}Fe source in the case of $ArCH_4$. Excited cerium is usually used in the case of $XeCH_4$. The calibration mechanism is explained in full detail in section 3, as an improvement of the energy calibration using $ArCH_4$ as counting gas, was part of this thesis. Particles that enter the active volume can ionize the counting gas and produce a certain number of electron-ion-pairs. The mean number of this primary ionizations is proportional to the energy deposition in the gas. Due

to the electric field the electrons will be accelerated towards the anode and the ions towards the cathode where they are collected [Leo]. In our case the high voltage is high enough that the electrons themselves are capable to ionize the counting gas and thus create secondary ionizations. In this way the interaction of an ionizing particles induces a current in the counter. It is transformed into an amplified and pulse shaped voltage signal which's height and time stamp is finally stored to disk. The high ionization density of an α-particle often saturates the amplifier and the corresponding event is stored in the overflow channel. Although information about the particles energy is lost the device can still be used for counting. A low energy cut is applied to reduce background arising from ambient radiation and electronic noise. Particles that depose an energy greater than the energy threshold are regarded as decays in the ^{222}Rn chain. Background spectra using different shieldings and counting gases are shown in section 4.

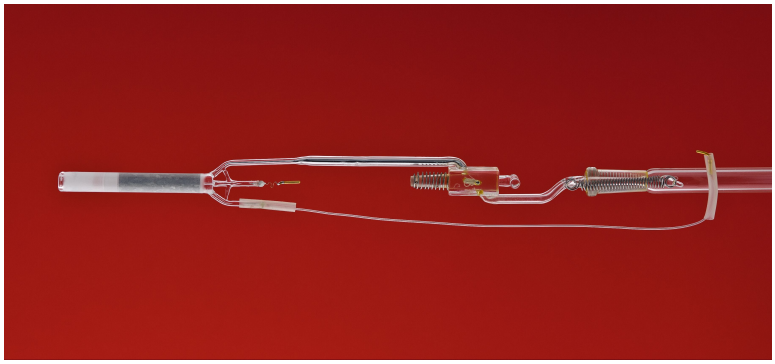

Figure 2.3: Miniaturized proportional counters used for the measurement of ^{222}Rn decays. It has a length of around 20 cm. The grey-shaded cylinder on the very left is the active volume with the cylindrical cathode. The sample is pushed into this volume with mercury.

Data evaluation

From the moment t_0 when the radon atoms are extracted the continuous production stops and the saturation equilibrium is broken. Only the decay of the ^{222}Rn atoms remains. Since one is interested in the saturation activity of the sample one has to deduce it from a decreasing activity measured with the proportional counters. The number of counts N_m measured within a time interval $[t_1, t_2]$ is given by

$$N_m = \int_{t_1}^{t_2} A_m \cdot e^{-\lambda \cdot t} \, dt \, , \tag{2.2.1}$$

whereby A_m is the measured activity of the sample at time t_1. The decay constant of ^{222}Rn is specified by λ. Here, the background contribution from the counter was omitted. From equation 2.2.1 one finds for the measured activity

$$A_m = \frac{N_m \cdot \lambda}{e^{-\lambda \cdot t_1} - e^{-\lambda \cdot t_2}}. \tag{2.2.2}$$

The activity A_m is related to the initial saturation activity A_0 at time $t_0 = 0$ via

$$A_m = \epsilon_{fill} \cdot \epsilon_{yield} \cdot \epsilon_c \cdot A_0 \cdot e^{-\lambda \cdot t_1}, \tag{2.2.3}$$

in a simplified manner when all blank contributions are neglected. They describe the constant contribution of radon atoms emanating from all the containers that included the sample during the measurement procedure. The additional ^{222}Rn atoms decay and contribute to the measured activity. Their contribution depends on the time difference when they were added to the sample and when data acquisition started. The efficiency ϵ_{fill} accounts for the loss of sample when filling the proportional counter. Another efficiency, ϵ_{yield} must be considered since the saturation activity is not completely reached within the time of radon emanation. The decay of ^{222}Rn induces a chain of subsequent decays until the daughter isotope ^{210}Pb is obtained. These decays are also detected within the proportional counter. Hence the actually detected number of counts exceeds the number of the radon atoms. This ratio is considered with the efficiency ϵ_c. At the recent threshold at channel 800 ($\sim 50\,\text{keV}$) the counter efficiency is $\epsilon_c = (1.47 \pm 0.06)\%$. This threshold is applied to reduce background. The value was determined as the average of several measurements with the counting gas $ArCH_4$. It means that for one ^{222}Rn decay ~ 1.5 counts are detected. The counter efficiency is determined with a sample of known activity, referred to standard. In chapter 5 the efficiency ϵ_c will be determined for the lower energy threshold with the best signal/noise ratio for different combinations of counting gas and applied shielding. In general one uses standards with a high activity ($\sim 200\,\text{mBq}$). Thus all blank contributions can be neglected in the calculation of ϵ_c as it was done in equations 2.2.1 - 2.2.3.

A full description of the general data evaluation including the blank contributions and efficiencies can be found in [32]. This algorithm was also implemented in a database based on PostgreSQL and with the possibility of web access. It allows for example a quick data evaluation, additional information on recorded spectra and an overview of all measurements done in the last decade.

2.3 ^{222}Rn emanation results of XENON1T

Every part of the XENON1T detector that is in contact with the target material, the liquid and gaseous xenon, has to be intensively screened in advance. The ^{222}Rn emanation measurements of the small sub-components were performed at MPIK. The large components like the cryostat or the crogenic system were not shipped to MPIK. They were rather extracted at the workshop of the fabricating company in Italy, Alca Technology S.r.l.[2], or directly at the construction side of XENON1T in the underground halls of LNGS. We used a mobile extraction system with a getter as shown in Fig. 2.2 for these measurements. The sample was stored in a trap and filled into a proportional counter at the permanently installed gasline at LNGS.

2.3.1 Results

1) Test Welds

During assembling of the detector many components are welded together. Since the resulting weld seams could also constitute a potential ^{222}Rn emanation source, samples of weld seams are investigated in advance to estimate their contribution to the total ^{222}Rn contamination. In [56] a measurement of steel plates is stated that were welded and afterwards electropolished. The result for the ^{222}Rn emanation rate is (100±4) μBq/m of weld seam under the assumption that only the weld seams emanate ^{222}Rn. Two different weld seam samples were tested during the ^{222}Rn emanation measurement campaign of XENON1T. The stainless steel tubes were electropolished after welding. Assuming that the ^{222}Rn emanates only from these weld seams a ^{222}Rn emanation rate of $(16 \pm 6)\,\mu$Bq/m and $(14 \pm 5)\,\mu$Bq/m weld seam was measured, respectively. These results present the lowest ^{222}Rn emanation rate for electropolished weld seams that were ever measured. They can be combined to an emanation rate of $(15 \pm 4)\,\mu$Bq/m weld seam.

More details on the investigated samples are given below. The two mentioned weld seam samples for XENON1T were either obtained from the company that fabricated the cryogenic system and the cryostat, respectively. Relevant for the actual contribution to the total ^{222}Rn contamination are the weld seam samples that were electropolished (labeld as sample B) in the following) as this is standard cleaning procedure for the stainless steel detector components of XENON1T.

[2] http://www.alcatechnology.com

a) Test welding of cryogenic system: We obtained 3 samples of tubes with weld seams from Lamm's Machine Inc., the company that fabricated the cryogenic system of XENON1T. Each sample consisted of a tube (30 cm length and 10 cm diameter) with 12 weld seams of 3.6 m total length. The difference of the samples were their surface treatment after welding. Sample A) did not undergo any cleaning procedure and the surface stayed untreated. Sample B) was electropolished and sample C) was electropolished and etched. The results of the measured, non-normalized activity A_M are given in Table 2.1. From this result the activities A_L and A_A were calculated by assuming on the one hand that the ^{222}Rn emanation originates from both, the surface and the weld seams of the particular tube and on the other hand that mainly the weld seams emanate ^{222}Rn. Sample A) did not show a detectable activity. For these welding samples no significant cleaning effect was observed.

label	treatment	A_M [μBq/m]	A_L [μBq/m]	A_A [μBq/cm^2]
A	no cleaning	< 47	< 13	< 0.08
B	electropolished	59 ± 23	16 ± 6	0.10 ± 0.04
C	electropolished and etched	67 ± 18	19 ± 5	0.11 ± 0.03

Table 2.1: Treatment and results of tubes with weld seams of cryogenic system: given are the non-normalized activity A_m, activity A_L per length of welding seam and activity A_A per area of tube.

b) Test welding of cryostat: Another investigation of test weldings was done with samples provided by Alca Technology. This company manufactured the cryostat and the pipes connected to it. We screened 3 tubes with in total 4.7 m of welding seams before any surface treatment (sample A)). The measurement was repeated after electropolishing exactly the same sample (sample B)). Moreover we investigated tubes of the same stainless steel without any welding or cleaning (sample C)). The results are shown in Table 2.2. The activity of the untreated tube and the one with non-cleaned weld seams agrees within the error (sample A) and C)). Electropolishing significantly lowered the ^{222}Rn emanation rate.

label	treatment	A_M [μBq/m]	A_L [μBq/m]	A_A [μBq/cm^2]
A	no cleaning	220 ± 27	47 ± 7	0.12 ± 0.01
B	electropolished	67 ± 22	14 ± 5	0.04 ± 0.01
C	no welding	173 ± 55	-	0.09 ± 0.03

Table 2.2: Treatment and results of tubes with weld seams of cryostat: given are the non-normalized activity A_M, activity A_L per length of welding seam and activity A_A per area of tube.

2) TPC components

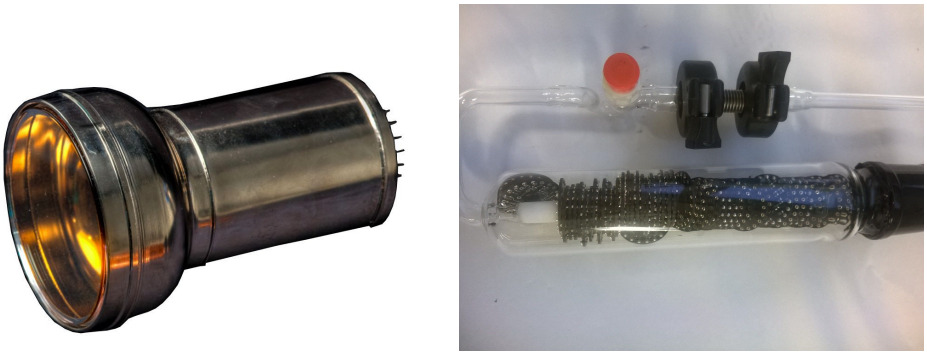

(a) ***(b)***

Figure 2.4: ***(a)*** R11410 PMT used to detect the scintillation light induced by particle interaction in the TPC. ***(b)*** Preliminary Cirlex PMT bases in a glass vessel, that serves as emanation container.

a) R11410 PMTs: For the measurement of the PMTs (Photomultiplier Tubes) we used neon as carrier gas instead of the usually used helium. The latter could diffuse into the PMTs and stay there leading to an increase of so-called after-pulses that could hinder the identification of WIMP dark matter particles. We investigate 29 PMTs with the total ^{222}Rn emanation rate of $(67 \pm 27)\mu$Bq. This results in a rate of $(2.3 \pm 0.9)\mu$Bq/PMT and an expected total emanation rate of (0.6 ± 0.2) mBq for the 248 PMTs used in XENON1T. A PMT is shown in Fig.2.4a.

b) Cirlex PMT bases: The preliminary version of these bases was measured with a result of $(3.0 \pm 0.6)\mu$Bq/base. They are shown in Fig.2.4b. The resistor will be exchanged for the actually used bases in XENON1T and the surface will become slightly bigger. From theses bases we expected a total emanation rate of (0.7 ± 0.1) mBq for 248 bases.

c) PTFE plates: PTFE (Teflon) will be used to encase the TPC of XENON1T because it provides a high reflection probability of UV light and accordingly scintillation light triggered by a potentially WIMP interaction. We investigated 61 Teflon plates with a total surface area of $\sim 4\,\mathrm{m}^2$ and a total weight of $\sim 32\,\mathrm{kg}$ that were cleaned with ethanol before the first measurement. The final non-normalized result is $(105 \pm 21)\,\mu\mathrm{Bq}$. Normalized to the surface and mass a ^{222}Rn emanation rate of $\sim (26 \pm 5)\,\mu\mathrm{Bq/m}^2$ and $\sim (3.3 \pm 0.7)\,\mu\mathrm{Bq/kg}$ was measured, respectively.

3) Components of purification system and heat exchanger

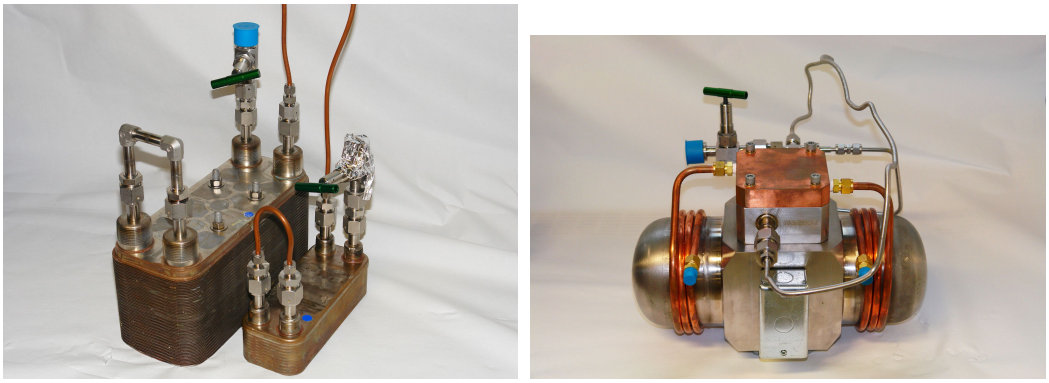

(a) *(b)*

Figure 2.5: ***(a)*** Heat exchanger will be used to evaporate and liquefy xenon in the recircurlation-purification loop. ***(b)*** In order to transfer xenon through the gas system of XENON1T QDrive pumps are used.

a) Heat exchanger: In 2013 a heat exchanger from our colleagues from Columbia University, New York was investigated, note also [32]. The interior of the heat exchanger was measured before any previous surface treatment and again after etching it with nitric acid diluted to 1.8 %. The ^{222}Rn emanation was reduced from $(0.49 \pm 0.06)\,\mathrm{mBq}$ for the untreated inner surface to $(0.12 \pm 0.02)\,\mathrm{mBq}$ for the etched one. In 2014 the same heat exchanger was measured again together with a smaller one. A picture of both connected heat exchangers can be seen in Fig.2.5a. The cleaning procedure before the measurement was more complex. The interior of both heat exchangers were connected and flushed with nitrogen. Afterwards they were evacuated and cleaned with a weak nitric acid solution of 1.8 %. The ^{222}Rn overall emanation rate is $(0.07 \pm 0.03)\,\mathrm{mBq}$. This investigation confirmed the hypothesis

that a weak nitric acid solution can be used for effective surface cleaning. This bases on the removal of ^{226}Ra from the surface of the investigated sample.

b) QDrive Pumps: Whereas XENON100 uses a KNF pump, XENON1T is foreseen to operate two QDrive piston type pumps as they are supposed to have a longer endurance, a better leak tightness and a larger pumping rate. An exemplar of a QDrive pump can be seen in Fig.2.5b. Polyester lacing fixes coils to a frame. The combination is called stator. This component is shown in Fig.2.6a. The stator is housed in a flexure assembly to fix it inside the QDrive. For pumping gas, pistons that couple permanently to magnets are moved electromagnetically. Epoxy is used to coat the magnets inside the QDrive. In 2014 we screened the two QDrive pumps that should operate in XENON1T. We determined a rate of (3.6 ± 0.2) mBq for the pump with the serial number C205 and (5.3 ± 0.2) mBq for the one with serial number C204. To find out which sub-component causes the rather high emanation rates we started to screen some individual parts separately. All recent results of the QDrive investigation are listed in Table 2.3. The overall rate of the individual measured sub-component is $(4.2^{+0.2}_{-0.1})$ mBq. This result is comparable with the average of (4.5 ± 0.1) mBq of the two measured QDrive pumps. The main contribution arises from the two stators with a total emanation rate of (3.0 ± 0.2) mBq.

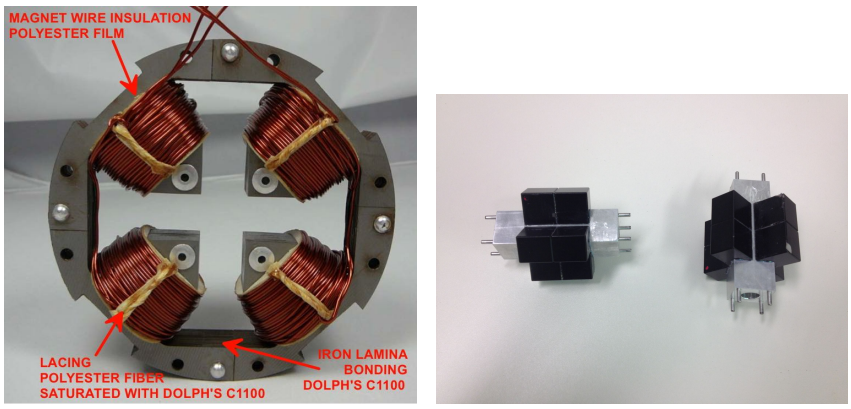

(a) *(b)*

Figure 2.6: ***(a)*** Stator of a QDrive piston pump. It contains the polyerster lacings that are saturated with Dolph's Epoxy resin and the magnet wire winding. ***(b)*** Magnets of the QDrive piston pump.

sample	activity [mBq]	comment
QDrive	3.6 ± 0.2	serial number: C204
QDrive	5.3 ± 0.2	serial number: C205
polyester lacings	< 0.05	8 pieces
Dolph's Epoxy resin CC1105	0.06 ± 0.02	3.6 g
magnet pairs with Epoxy	0.019 ± 0.002	4 pieces
screws and smaller components	< 0.02	[3]
magnet wire winding	< 0.1	~ 1 kg
piston	0.70 ± 0.07	2 pieces
magnet	0.3 ± 0.1	16 pieces
flexure assembly	0.16 ± 0.02	4 pieces
stator	3.0 ± 0.2	2 pieces

Table 2.3: Individual emanation results of QDrive and its sub-samples.

c) Getter: Two noble gas getters of the type PS4-MT50-R-2 of the company SAES were investigated. Both getters will be used in the purification system. The getter was at its (hot) operating temperature during extraction. For one of the getters we measured (1.3 ± 0.1) mBq whereas for the other one we obtained an emanation rate of (0.26 ± 0.03) mBq, which is significantly lower. The reason for this discrepancy is not understood and requires further screening effort.

4) Individually measurements of gas system components

a) 100mm Pipe: As mentioned in chapter 1.2.2 the 100 m pipe contains cables for the PMT supply. Fig. 2.7b shows these cables [4]. Before the first extraction they were cleaned with ethanol, bunched together and finally inserted into the pipe. The pipe was pumped and baked for one week to reduce the amount of outgassing from the cables. The first measurement was done in the workshop of Alca Technology and the other two at the construction side of XENON1T at LNGS, after mounting the pipe inside the water tank. The result of each measurement is given in Table 2.4 as well as the final result that is obtain by averaging over them. The expected emanation rate from the individual components inside the pipe gave an upper limit of < 4.4 mBq[5] that is consistent with the final result.

[3] 2 axis screws, 1 epoxy sample DP460E6, 1 epoxy sample CE-211R, 1 Formular 8, 8 screws, 8 nuts, 8 SS plates, 12 spacers

[4] The tube on the picture was only used for testing the insertion into the 100 m pipe.

[5] In the calculation of the upper limit the emanation rate of Teflon cables from another producer were used. We expect a similar emanation rate for the cables that are inside the pipe.

(a) *(b)*

Figure 2.7: ***(a)*** Cryostat of XENON1T. Picture was taken during emanation measurement in the workshop of Alca Technology. One can also see the green bottle containing the carrier gas and parts of the mobile emanation system. ***(b)*** The 100 m pipe contains ~ 8.7 km cables that partly shown here. The tube at the picture was used for testing the later insertion of the cables into the 100 m pipe.

date of counter filling	activity [mBq]
20.06.2014	2.3 ± 0.2
08.08.2014	3.1 ± 0.2
23.08.2014	2.6 ± 0.2
combined result	2.7 ± 0.2

Table 2.4: Individual emanation results of the 100 mm pipe and the combined result.

b) Feedthrough vessel: This vessel is mounted at the external side of the 100 mm pipe and serves as feedthrough for the cables. The emanation rate of its inner surface is (1.9 ± 0.2) mBq.

c) Cryostat: The measurement of the cryostat was also done at the workshop of Alca Technology. A picture of it can be seen in Fig.2.7a. It was taken during the emanation measurement and shows also parts of the mobile emanation system. The cryostat has a volume of $\sim 2\,\mathrm{m}^3$. Due to this large volume and the slow extraction speed only half of the filled carrier gas was extracted. The obtained emanation rate was afterwards scaled up by a factor of ~ 2 to the entire volume. The measurement was done one time with a result of (1.9 ± 0.3) mBq. The emanation measurement of the

cryostat was essential for the further measurement campaign as some of the detector parts were only investigated in combination with the volume of the cryostat. Their particular emanation rate is constrained by the emanation rate of the cryostat.

d) Main part of cryogenic system: The major part of the cryogenic system was measured with the average result of (2.4 ± 0.3) mBq. We expect that the emanation rate of the missing parts to be small in comparison to this result.

e) Purification system: The measurement of the purification system includes the inner surface of the previously measured two getters and the two QDrive pumps. The getters were hot during the extraction whereas the pumps were off. The pneumatic valves of the system were set as during operation mode of XENON1T. We expect a rate of (10.4 ± 0.3) mBq from the getters and QDrives. The measured emanation rate is (7.3 ± 0.9) mBq. The expectation and the actually measured emanation rate are not in agreement. Some volumes of the purification system were maybe not accessible during the measurement that include some radon sources. This could be an explanation for the lower result of the actual measurement.

5) Combined measurements of gas system components

a) Cryostat and pipes: After measuring the cryostat alone it was shipped to LNGS and connected to the 250 mm pipe. In advance the 100 m pipe and thinner pipes were inserted into the 250 mm pipe. This entire system was mounted in the water tank of XENON1T as can be seen on Fig.2.8. The measurement contained the inner surface of the 250 mm pipe and of the cryostat as well as the inner and outer surfaces of the thinner pipes . The 100 mm pipe was sealed and only its outer surface contributed to the emanation rate. Three measurements were done in this configuration. Table 2.5 shows their individual results as well as the averaged emanation rate.

After measuring the rather high emanation rate of (14.2 ± 0.6) mBq the question was posed which component is causing it. Only the cryostat was measured individually with a emanation rate significantly lower than the one of the cryostat+pipe system. Different potentially emanation sources were investigated that are listed in the following:

Figure 2.8: The picture shows the cryostat as it is mounted to the transport pipe. The top of the outer vessel is already installed but the vessel itself will assembled later. The entire system of cryostat and pipes is installed inside the water tank.

date of counter filling	activity [mBq]
22.08.2014	15 ± 1
04.09.2014	13 ± 1
10.09.2014	14 ± 1
combined result	14 ± 1

Table 2.5: Individual emanation results of the cryostat+pipe system before modification and the combined result.

- **air leak:** an obvious cause for the high emanation rate could be an air leak that leads in turn to a diffusion of ambient radon into the cryostat-pipe system. However this hypothesis was excluded after several thoroughly leak checks.

- **bellows:** another hypothesis was that the bellows of the thin pipes inside the 250 mm pipe are contaminated. These bellows are concertina-like stainless steel parts of the pipe that compensate the deformation of it due to normal pressure changes. In contrast to the other parts of the system these bellows were not electropolished in advance due to technical reasons. The inner and outer surface of a non-electropolished test bellow with a length of 1 m and diameter of 3.5 cm was measured. It was provided by Alca Technology and the result is (0.16 ± 0.03) mBq. Even after scaling this result up to the total length of bellows inside the system it cannot explain the the

high emanation rate. Moreover an electropolished bellow was investigated as cross check. It has a length of 40 cm and a diameter of 10 cm and was used as end-cap for sealing the 100 mm pipe. The emanation result of the inner surface only is (0.12 ± 0.03) mBq.

- **valves:** two valves that were included in the previous measurements of the cryostat + pipe were removed for a subsequent measurement of this system. One of them closed the 100 mm pipe and hence its outer surface contributed to the emanation rate. It was completely removed. The other served as a second port for the 250 mm pipe and so its inner volume was included in the cryostat+pipe measurement. It was replaced by a full metal valve.The emanation rate of the modified cryostat+ pipe system is (11 ± 1) mBq.

The emanation result of the modified cryostat+pipe system is lower after removing the two valves. An emanation rate of (9 ± 1) mBq can be assumed for the pipes only, if one subtracts the emanation rate of the cryostat from the one of the modified system. The rather high emanation rate for the pipes is not understood.

b) Cryostat, pipes and cryogenic system: This measurement includes

- the inner surface of the 250 mm pipe,
- the inner and outer surface of the 100 mm pipe containing the PMT cables,
- the inner and outer surface of the thin pipes inside the 250 mm pipe,
- the inner surface of the cryostat,
- the inner surface of the feedthrough vessel and
- the inner surface of the cryogenic system (all parts).

The rather large and nested volume carries the risk that the emanated radon atoms are not distributed homogeneously. This could lead to a distorted result for the total emanation rate if not all of the carrier is extracted as it was done in this measurement. Therefor the measurement procedure was slightly changed. The total system was only filled with roughly two-third of the usual carrier gas amount in the step of preparation. Before extraction the volume was filled with more carrier gas to circulate the already existing gas and the emanated radon atoms and provide a homogeneous mixture. The measured emanation rate is

(14 ± 1) mBq. This is smaller than the expectation of the mentioned sub-samples with a combined emanation rate of (18 ± 1) mBq. The measured emanation rate for the combined system is significantly lower than the expectation from the sub-components. An explanation could be that radon sources are present in volumes that are difficult to access and hence that the radon was not distributed homogeneously in the entire system.

2.3.2 Summary of ^{222}Rn emanation results

Table 2.6 presents the summarized results of all described ^{222}Rn emanation measurements. From these results one can estimate a total ^{222}Rn emanation rate of the entire investigated system. The emanation rate resulting from the PTFE was neglected in this calculation. A transfer of the measured emanation rate of 61 plates to the complex PTFE housing of the TPC is non-trivial. It is not clear if the ^{222}Rn contamination scales with the surface or if the ^{222}Rn could also diffuse from deeper lying layers within the PTFE to the outside. By summing up the samples 2 - 12, referred in Table 2.6 (except of the PTFE with the number 4), a total ^{222}Rn emanation rate of $A_{ind.} = (30 \pm 1)$ mBq is reached. This calculation considers the results of the individual components. The emanation rate of the 250 mm pipe with the included thin pipes was deduced from the difference in the emanation rate of the cryostat+pipe system and the cryostat only. By summing up the emanation rate resulting from the measurements of the combined components, described in 5), and the total contribution from the PMT, the PMT bases and the heat exchanger, we obtain a total emanation rate of $A_{comb.} = (24 \pm 1)$ mBq for the entire system. The discrepancy of $A_{ind.}$ and $A_{comb.}$ could arise from the inhomogeneous distributed radon atoms in the nested volume of the gas system. As one did not extract the entire volume, parts with a higher radon contamination could misleadingly less contribute to the overall rate. In the next section a conclusion on these results is given.

number	sample	activity [mBq]	comment	text ref.
1	electropolished test weld	0.015 ± 0.04/m	combined result	1)
2	PMTs	0.6 ± 0.2	248 pieces	2a)
3	PMT bases	0.7 ± 0.1	248 pieces	2b)
4	PTFE	0.11 ± 0.02	61 plates	2c)
5	heat exchangers	0.07 ± 0.03	-	3a)
6	QDrive pumps	8.9 ± 0.3	-	3b)
7	getters	1.6 ± 0.1	-	3c)
8	100 mm pipe	2.7 ± 0.2	-	4a)
9	feedthrough vessel	1.9 ± 0.2	-	4b)
10	cryostat	1.9 ± 0.3	-	4c)
11	cryogenic system	2.4 ± 0.3	-	4d)
12	250 mm pipe and thin pipes	9 ± 1	-	5a)
13	purification system	7 ± 1	-	4e)
14	cryostat + pipes	11 ± 1	-	5a)
15	combined main parts	14 ± 1	-	5b)

Table 2.6: Summarized ^{222}Rn emanation results of XENON1T.

2.4 Conclusion

^{222}Rn is a potential background source in experiments dealing with a low event rate. It emanates permanently from almost all materials. During its rather long half-life of $T_{1/2}^{Rn222} = 3.82$ days the noble gas can reach the active volume of the detector before disintegration. Amongst its daughter isotopes the β-decay of ^{214}Pb turns out to be most critical background contribution in the energy region relevant for dark matter search [19].^{222}Rn has the potential to be one of the limiting factors on the sensitivity of XENON1T. One strategy to minimize the radon background is a careful selection of detector materials with a low ^{222}Rn emanation rate. In section 2.2 we explained the procedure of the ^{222}Rn emanation measurements.

The results of the ^{222}Rn measurement campaign for XENON1T are discussed in section 2.3. We investigated welds seam samples, since many of the detector parts are welded together during assembling. To our knowledge, we obtained the lowest limit for electropolished welds seams that were ever measured, with a result of $(15 \pm 4)\,\mu$Bq/m weld seam. Furthermore we saw that already a weak nitric acid solution can be used for cleaning metal surfaces, resulting in a lowered ^{222}Rn emanation emanation rate. This could be explained by the removal of the ^{222}Rn mother nuclei, ^{226}Ra, from the surface.

By adding up the the emanation rates of the XENON1T components, that were measured in combination with other parts of the detector, we obtain an overall ^{222}Rn emanation rate of $A_{comb.} = (24 \pm 1)$ mBq. This result is significantly lower as the emanation rate that can be deduced by summing up the ^{222}Rn emanation rate of the same components but measured individually. The overall emanation rate of this method is $A_{ind.} = (30 \pm 1)$ mBq. The discrepancy of $A_{comb.}$ and $A_{ind.}$ could be explained by a inhomogeneous radon concentration in the case of measurements of the combined systems, due to its nested volume. Since not all of the volume was extracted, radon atoms that might be accumulated in smaller subvolumes that are difficult to access, are not extracted. This could misleadingly lower the overall measured ^{222}Rn concentration.

Fig. 2.9 shows the relative fractions of individual results constituting $A_{ind.} = (30 \pm 1)$ mBq. From the diagram two main sources of ^{222}Rn contamination are identified: the 250 mm pipe containing thinner pipes and the QDrive pumps. The combined emanation rates of these two components make up $\sim 60\,\%$ of the overall

rate, whereby both contribute nearly with the same amount. The 250 mm pipe with the included thin pipes was reinvestigated after measuring the ^{222}Rn rate of (9 ± 1) mBq. No distinct radon source, causing this rate, could be identified so far. The origin for the rather high emanation rate of the QDrive pumps is more clear. The stator, a frame for fixing the coils and magnets inside the pump, accounts for almost 60 % of the ^{222}Rn emanation rate of both pumps. This result requires further investigation. One could consider the exchange of the materials that are causing the high rate, especially for the future project XENONnT.

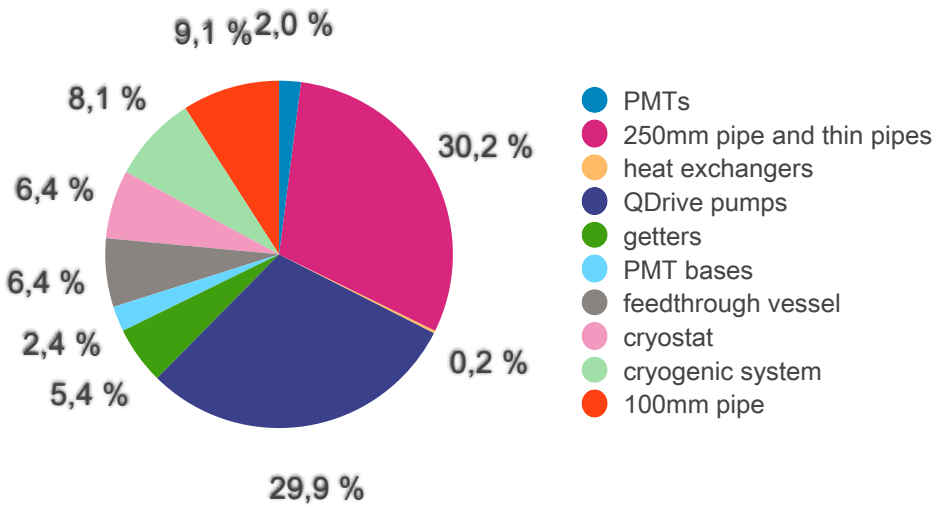

Figure 2.9: Relative fractions of the ^{222}Rn emanation rates arising from the single components of the XENON1T detector.

The measured overall emanation rate exceeds the XENON1T goal of $\sim$ 3 mBq in $\sim$ 3.3 tons of liquid xenon. The emanation rate was measured under different thermal conditions as they are present the in the liquid xenon with a temperature of $\sim$ 180 K. Hence a transfer of the measured contamination to the one that might be present in the liquid xenon is more complex. The measured rate indicates that radon could become the dominant intrinsic background source in XENON1T. Therefor sophisticated analysis tools were developed for the discrimination of radon induced background and signal, leaned on the analysis that was already applied in XENON100. Moreover purification systems that could remove radon from xenon are under investigation. Recent investigations on the separation of xenon and radon, performed within the XENON1T collaboration, showed promising results.

Chapter 3

Energy calibration of proportional counters

In order to compare spectra measured under different conditions an energy calibration is necessary. The variation of pre-amplifier voltages of different setups or measurements done with different counters could influence the position of the spectra that is stored in units of channel. Depending on the noble gas component of the counting gas, different calibration sources are used in daily work. For $ArCH_4$ we usually use ^{55}Fe whereas cerium serves for the the calibration of $XeCH_4$. Since cerium induces well known energy depositions in xenon over a large range (up to $\sim 39\,keV$) it also allows testing the energy scale's linearity. One goal of this work is to compare the counting gases $ArCH_4$ and $XeCH_4$ with one another and to ascertain if they have different efficiencies in the detection of radon decays. Furthermore background spectra of proportional counters with different shielding and the two different counting gases will be compared. This makes a calibration of $ArCH_4$ over a larger energy range necessary. One calibration method for this has been developed and tested in this work.

3.1 Calibration technique

Both, the calibration with excited cerium and with the decay of ^{55}Fe follows the same main principles. The used calibration sources produce discrete x-rays in the keV range. In this energy range the photoelectric effect is the most dominant process of photon absorption. Fig. 3.1 shows the absorption lengths of photons in different noble gases. Thereby standard conditions of temperature and pressure are considers, that are given in our measurements. Whenever the energy of the photon is high enough to eject an electron from a deeper lying shell of the atom

the cross section of photon absorption is increasing rapidly.

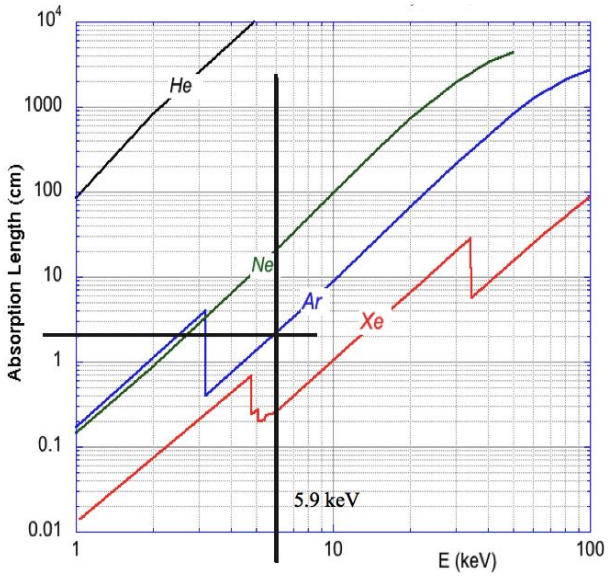

Figure 3.1: Absorption lengths as a function of photon energy for various noble gases under standard conditions. Picture taken from [43].

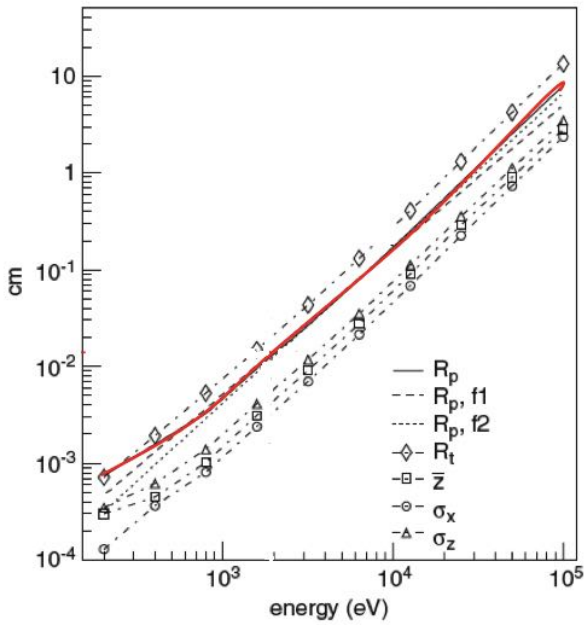

Figure 3.2: The red line shows the electron range as function of the electron energy in argon under standard conditions. Picture taken from [47].

Hence the absorption lengths decreases leading to the characteristic sawtooth absorption edges. Depending on the initial x-ray energy of the calibration source and the binding energies of the different atomic shells, atoms are ionized. The resulting hole is filled with an electron from a higher shell. Thereby energy is released via fluorescence x-rays, Auger electrons or Koster-Croning transmission. The probability for each of these modes to occur depends on the ionized shell and the element. They are shown in Fig. 3.3 for the ionization of the K, L_1, L_2 and L_3 shells, respectively.

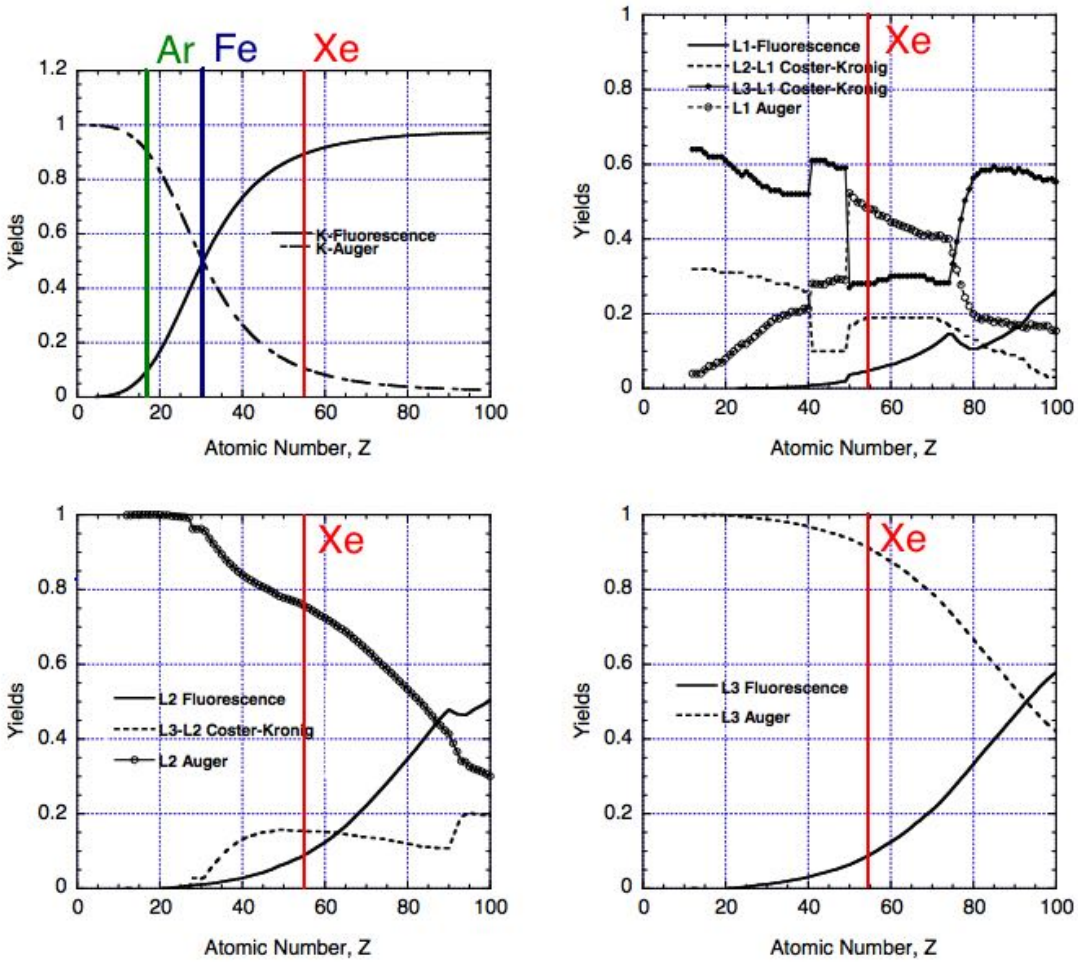

Figure 3.3: Probability of fluorescence x-rays, Auger electrons or Koster-Croning transmission after photoionization depending on the ionized shell and element. The colored lines indicate the relevant shells that could be ionized due to the calibration sources described in the text . Picture taken from [40].

The cylindrical active volume of the proportional counters have a diameter of around 0.5 cm and a length of around 3 cm. This means that the fluorescence x-rays and Auger electrons have in principal the chance to leave the counter without being detected. For example the fluorescence x-rays released after the ionization of the xenon's K-shell can have energies up to $\sim 30\,\mathrm{keV}$ and a range of $\sim 20\,\mathrm{cm}$. This exceeds the dimensions of the active volume. The Auger electrons however have much smaller absorption lengths. Fig. 3.2 depicts the absorption lengths of electrons as a function of their energy in argon. In the subsequent discussed calibration methods the Auger electrons never exceed an energy of $\sim 30\,\mathrm{keV}$. This would cause a range of $\sim 1\,\mathrm{cm}$ in argon. They lose their energy mainly by ionization of valence electrons and the magnitude of the energy loss is amongst others proportional to the atomic number Z of the traversed medium [35].Consequently the absorption length of electrons in xenon is much smaller than in argon at the same electron energy. Thereby their detection probability is higher. Nevertheless the electrons do still have a small probability to leave the counter undetected or to be stopped at its walls. In these cases they do not contribute to the signal.

In the following sections the calibration of $ArCH_4$ and $XeCH_4$ is studied using x-rays of cerium and the decay of ^{55}Fe. First of all the calibration sources themselves are presented followed by a more detailed description of their energy depositions in both counting gases.

3.2 ^{55}Fe x-ray source

^{55}Fe decays via electron capture

$$^{55}\mathrm{Fe} + \mathrm{e}^- \rightarrow\ ^{55}\mathrm{Mn} + \nu_\mathrm{e} \tag{3.2.1}$$

whereby the electron is most likely captured from the K-shell of Fe. The resulting hole is filled by an electron from a higher shell and energy is released in form of x-rays. They are used for calibration by directing them to the active volume of the proportional counter. The most dominant emission lines are listed in Table 3.1 with their characteristic energies $\phi_i = \mathrm{E}_{\gamma-\mathrm{Fe}}$ and their intensities I_i relative to most intense emission line $\mathrm{K}_{\alpha 1}$. Since the single emission lines are not resolvable with the proportional counter, one can combine them to a group line with the average energy ϕ by using

$$\phi = \sum_i \ \frac{\phi_i \cdot \mathrm{I}_i}{\mathrm{I}_\mathrm{tot}} \tag{3.2.2}$$

and $I_{tot} = \sum_i I_i$. The result for ^{55}Fe is $\phi = 5.95\,keV$.

	^{55}Fe	
transission	$E_{\gamma-Fe}$ [keV]	I_i [a.u.]
$K_{\alpha 2}$	5.89	50.30
$K_{\alpha 1}$	5.89	100.00
$K_{\beta 3}$	6.49	5.98
$K_{\beta 1}$	6.49	11.72
$K_{\beta 5}$	6.54	0.01

Table 3.1: Emission lines of ^{55}Fe decay with corresponding energies $E_{\gamma-Fe}$ and relative intensities. Data taken from [61].

3.2.1 ^{55}Fe spectrum in $ArCH_4$

X-rays with the energies of $E_{\gamma-Fe}$ most likely eject the innermost argon electrons having a binding energy of $E_{K-Ar} = 3.2\,keV$ [62]. The ionization electrons carry off the energy $E_{PE-Ar} = E_{\gamma-Fe}$ - E_{K-Ar} which they lose again by moving through the counting gas. Thereby they could create further ionization mainly by interaction with valence electrons. The number of the resulting ionization electrons is proportional to the energy E_{PE-Ar} . The created hole in the K-shell of argon is filled by an outer-shell electron accompanied by the emission of Auger electrons but also in a small fraction by fluorescence x-rays as one can see on Fig. 3.3. This emission accounts for the remaining energy $E_{remaining} = E_{K-Ar}$ [27]. If $E_{remaining}$ is totally absorbed within the active volume, then the entire energy

$$E_{\text{full absorption}} = E_{PE-Ar} + E_{remaining} = E_{\gamma-Fe} \tag{3.2.3}$$

of the initial x-ray is detected. However there is also the probability that $E_{remaining}$ is not absorbed. The fluorescence x-rays have energies below the K absorption edge of argon. They could escape from the active volume as they have a large range in argon. If they do not depose their energy in the active volume, a peak in the pulse hight spectrum is left at

$$E_{escape} = E_{PE-Ar} \tag{3.2.4}$$

that is called the escape peak. The larger part of Auger electrons released in the disexcitation has in principle a greater probability to be detected. The exact intensity of the escape peak is depending on the geometry between the counter

and calibration source. It is not used for calibration. The full absorption peak however is suitable for calibration. A typical spectrum of the ^{55}Fe x-ray source in $ArCH_4$ is shown in Fig. 3.4 with the full absorption peak at $\phi_{Fe55} = 5.95\,keV$.

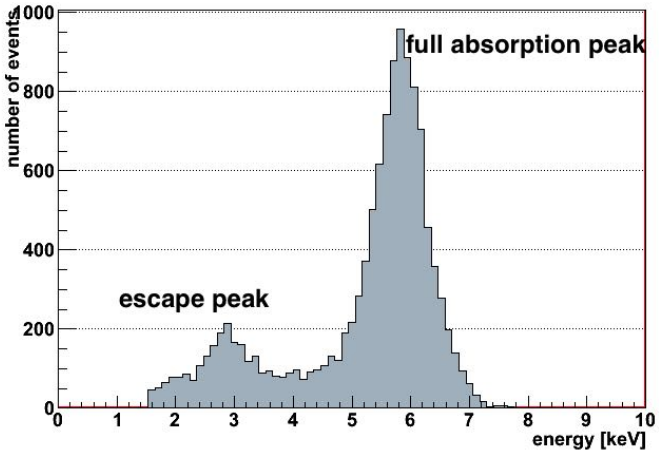

Figure 3.4: Spectrum of $ArCH_4$ irradiated with ^{55}Fe x-ray source.

3.2.2 ^{55}Fe spectrum in $XeCH_4$

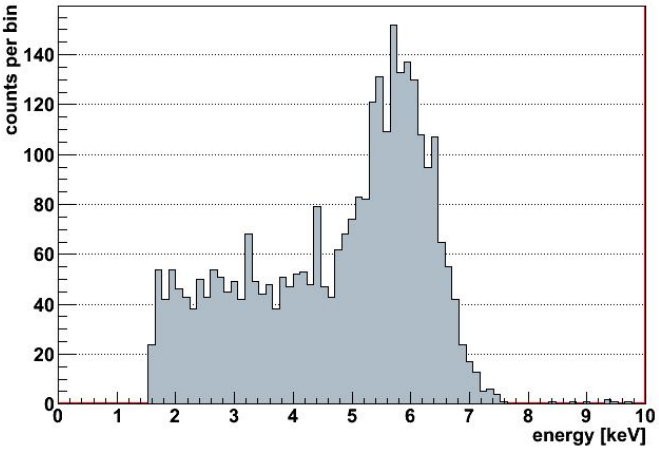

Figure 3.5: Spectrum of $XeCH_4$ irradiated with ^{55}Fe x-ray source.

The x-rays of the ^{55}Fe source can only ionize the L-shell or outer lying shells of the xenon atoms. The highest binding energy of $E_{L-Xe} = 5.4\,keV$ for the electrons on the L-shell [62]. The ionization results in the emission of mainly

Auger electrons. They could form the full absorption peak. A typically energy spectrum of $XeCH_4$ irradiated with ^{55}Fe x-ray source can be seen in Fig.3.5. In contrast to spectrum in $ArCH_4$ there are much more events at smaller energies and no escape peak is visible. The range of x-rays in xenon is smaller than in argon and the so they could be already stopped in the front part of the counter. In this region the electric field is distorted and the gas multiplication is lower. Consequently the energy of the events seems to be lower [44].

3.3 Cerium x-ray source

A cerium target is irradiated by an external x-ray source whereby cerium atoms can get ionized. The remaining holes are again filled with electrons from higher shells. Energy is released in the form of x-rays that can be used to calibrate counting gases. Cerium is a useful calibration source because it turns the continuous spectrum of the initial source into a discrete x-ray spectrum that offers some intense emission lines. These lines can basically be combined in three groups with the average energies of around 5 keV, 34 keV and 39 keV [61]. The 5 keV group line has an intensity of $\sim 10\,\%$ relative to the high energetic lines. The calibration mechanism, based on the absorption of the high energetic x-ray lines at 34 keV and 39 keV, is adapted from the work of [51].

3.3.1 Cerium spectrum in $XeCH_4$

Most important for the calibration of $XeCH_4$ are nine out of ten high energetic emission lines of cerium that are stated in Table 3.2. Their energies $E_{\gamma-Ce}$ exceed slightly the K-absorption edge of xenon with $E_{K-Xe} = 34.6\,keV$. Thus the cross section for the photoelectric effect is high. The K-absorption edge describes in general the energy E_K that is required to eject an electron from the K-shell. The ejected photoelectrons carry off the energy $E_{PE-Xe} = E_{\gamma-Ce}$ - E_{K-Xe} as indicated with green lines in Fig. 3.6. The created hole of the K-shell in xenon is filled with an electron of a higher shell by emitting most likely x-rays (see again Fig. 3.3). They have the energies $E_{\gamma-Xe}$. This radiation escapes usually from the active volume due to its large range and stays consequently undetected.

	cer		xenon	
transission	$E_{\gamma-Ce}$	rel. intensity	$E_{\gamma-Xe}$	rel. intensity
$K_{\alpha 2}$	34.279	54.7	29.459	54.1
$K_{\alpha 1}$	34.720	100	29.779	100
$K_{\beta 3}$	39.170	9.7	33.564	9.39
$K_{\beta 1}$	39.258	18.8	33.625	18.2
$K_{\beta 5/1}$	39.542	0.115	33.875	0.092
$K_{\beta 5/2}$	39.560	0.157	33.889	0.127
$K_{\beta 2/1}$	40.222	2.06	34.409	1.88
$K_{\beta 2/2}$	40.239	3.99	34.418	3.65
$K_{\beta 4/1,2}$	40.338	0.057	34.498	0.041
$K_{\beta 2/3,4}$	40.428	0.862	34.552	0.67
absorption edge	$E_{K-Ce} = 40.443$		$E_{K-Xe} = 34.561$	

Table 3.2: Emission lines of xenon and cerium with their energies stated in keV and relative intensities to the particular most intense line of the emission spectrum [50] .

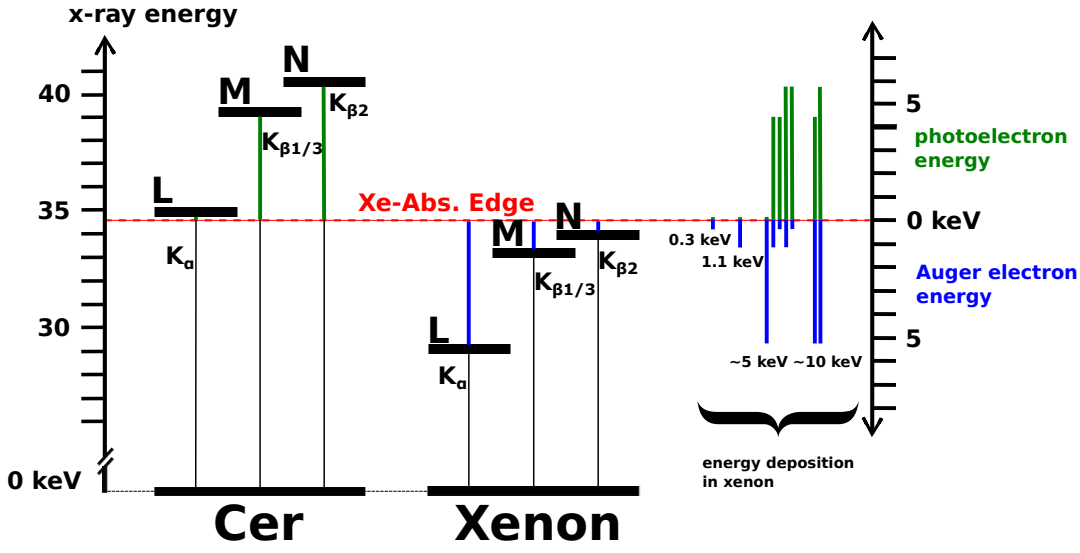

Figure 3.6: The picture shows the cerium conversion mechanism in xenon. The cerium emission lines eject electrons from the xenon K-shell leading to photoelectrons with energies indicated by green lines. These energies can add up with the energies of Auger electrons released by disexcitation processes within xenon and presented by blue lines. The conversion mechanism leads to four main groups of energy deposition in the counter's counting gas at around 0.3 keV, 1.1 keV, 5.1 keV and 9.8 keV. The picture is adapted from [51].

The remaining hole in the higher shell is again filled by an electron. This time the released energy is most likely transferred to a weakly bound electron of xenon that gets thereby ejected. Since this process leaves another hole it can be repeated several times. The resulting Auger electrons are detected with a total energy of $E_{Auger} = E_{K-Xe}$ - $E_{\gamma-Xe}$. Their energy is represented by blue lines in Fig. 3.6.In summary the total deposed energy of the electrons is

$$E_{tot} = E_{PE-Xe} + E_{Auger} = E_{\gamma-Ce} - E_{\gamma-Xe} \ . \tag{3.3.1}$$

There are nine high energetic emission lines of cerium that have enough energy to eject an electron from the K-shell of xenon. Ten different electron transitions are possibly within xenon, that could fill the hole. The resulting hole in the higher shell is again filled by an electron, whereas the released energy is transferred to Auger electrons. This means that for the nine possibilities of the energy E_{PE-Xe} there are ten possibilities of E_{Auger}. Consequently ninety lines are generated in xenon. They have energies in the range from 0.17 keV to 10.97 keV. The theoretical lines with the particular relative intensities are shown in Fig. 3.7. These lines can be combined to four main groups with the average energies of 0.29 keV, 1.11 keV, 5.10 keV and 9.76 keV by using again Eq. 3.2.2. Since the energy of the initial cerium x-ray is converted into electrons with a lower total energy the described process is called conversion.

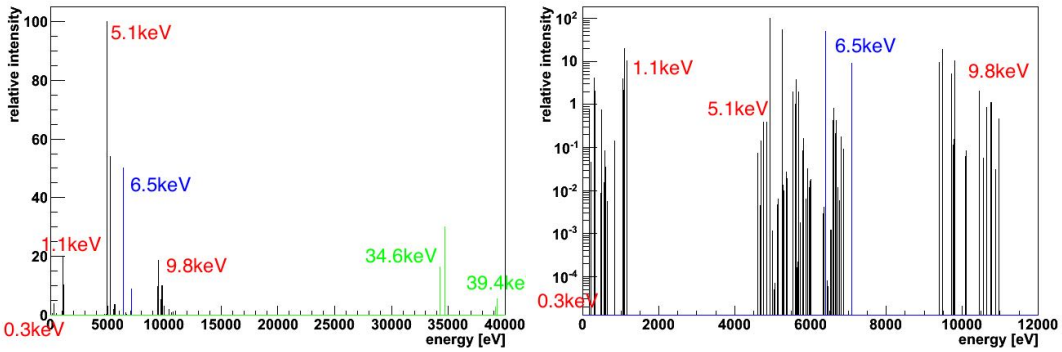

Figure 3.7: This figure shows a theoretical spectrum of cerium emission lines in $XeCH_4$. On the left side the spectrum is shown in full range whereas the right figure shows the spectrum in logarithmic scale of the converted lines. There are four main groups of just the converted lines with average energies of 0.29 keV, 1.11 keV, 5.10 keV and 9.76 keV, respectively. The green lines represent the non-converted lines at 34.56 keV and 39.43 keV. In blue the potentially energy deposition caused by the excitation of the counter's iron cathode is shown.

However, not all of initial cerium x-rays lead to this process. There is also a small probability that after the ionization of the xenon's K-shell the disexcitation energy not released as fluorescence x-rays but via Auger electrons. They have a greater chance to be detected. Together with the energy deposition of the photoelectrons this results in in full absorption peaks. They can again be clustered in two groups with average energies of 34.6 keV and 39.4 keV. A theoretical spectrum of the conversion peaks and the full absorption peaks can be seen in Fig.3.7 on the right side. A measured spectrum of $XeCH_4$ irradiated with cerium can be seen in section 3.4.1 in Fig. 3.10. In this section the calibration of $XeCH_4$ with cerium is discussed.

Iron Cathode

Some of the proportional counters possess a cathode made out of iron. The innermost electron of iron with a binding energy of 7.1 keV [61] could get ejected. The energy of the disexcitation process is equiprobably transferred to Auger electrons or released as fluorescence x -rays (note again Fig. 3.3). The four most dominant K x-rays of iron have an average energy of 6.5 keV that is visible in energy spectrum if the full energy is deposed. Its absolute intensity and the discrimination between this line and the converted line of cerium at 5.1 keV strongly depends on the irradiation geometry. The line originating from iron is presented in blue in the theoretical spectrum shown in Fig.3.7.

3.3.2 Cerium x-ray spectrum in $ArCH_4$

Fig. 3.8 shows a typical spectrum $ArCH_4$ irradiated by a cerium x-ray source. Cerium offers some high energetic emission lines at ~ 40 keV but since they have a large range in argon they most likely leave the active volume without being detected. Hence there are no full absorption peaks at these energies and cerium is not suitable to calibrate $ArCH_4$ over a large energy range. Moreover there are also no converted lines as in $XeCH_4$ since the premise for their creation is exactly the absorption of the high energetic cerium emission lines. The low energetic x-rays grouped at 5.12 keV however have a higher probability to be absorbed by argon. They could ionize the K-shell electron with a binding energy of $E_{K-Ar} = 3.2$ keV which is most likely followed by the emission of Auger electrons that are in turn detected by the counter. Their energy is deposed up to an energy range of ~ 5 keV. Another contribution arises from disexcitation of the iron cathode that leads to energy depositions at 6.5 keV.

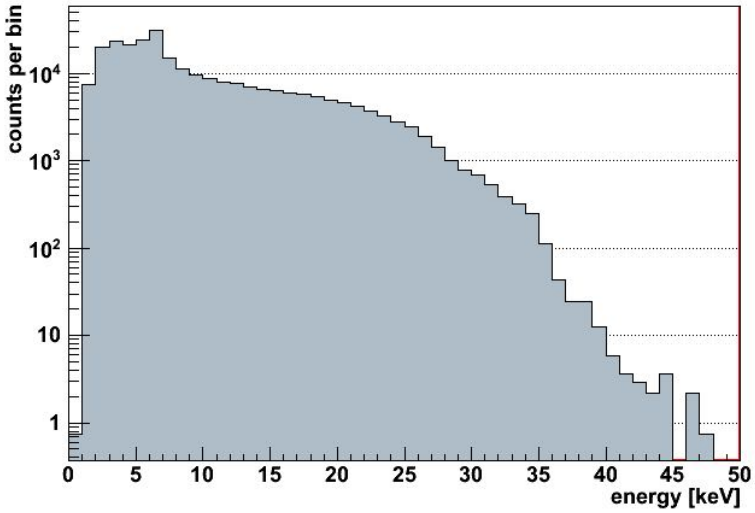

Figure 3.8: Spectrum of $ArCH_4$ irradiated with a cerium x-ray source. The range of the cerium x-rays at 34.6 keV and 39.4 keV is high in $ArCH_4$ and thus there are not detected.

In section 3.4.2 a procedure was developed to calibrate even $ArCH_4$ over a large energy scale like $XeCH_4$. A small amount of xenon atoms was admixed that should serve as a target for the high energetic x-rays of cerium. They ionize mainly the admixed xenon atoms whereby the resulting ionization electrons depose their energy mainly in the more abundant $ArCH_4$. Thereby the same energies are deposed in $ArCH_4$ as they were described in section 3.3.1 . Fig. 3.9 shows the normalized spectra of $ArCH_4$ with the admixture of 2 %, 5 % and 10 % xenon. With bare eyes one can see that the amount of xenon does not shift the positions of the 5.1 keV, 9.8 keV, 34.6 keV and 39.4 keV peak significantly[1]. The lower the amount of xenon the lower is the absolute event rate and intensity of the single peaks. It is conspicuous that the spectra have a similar decline at high energies as pure $ArCH_4$ irradiated with cerium x-rays. The similar shape leads to the assumption that the energy of the calibration electrons produced in xenon is mostly deposed in $ArCH_4$. In section 3.4.2 this assumption will be tested.

[1] the peaks at 0.3 keV and 1.1 keV are not resolvable at the high voltage that was used to record the shown spectrum

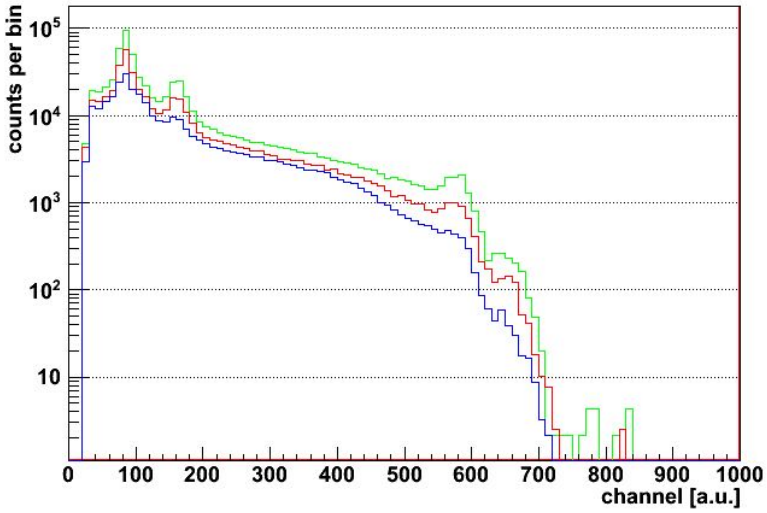

Figure 3.9: Spetrca of cerium x-rays in $ArCH_4$ with admixture of 2 % (blue), 5 % (red) and 10 % (green) xenon, respectively.

3.4 Multiple Line Fit

As we saw in the previous sections the main peaks of the spectra are actually a combination of multiple lines with different intensities. Each of them has to be included in the so called multiple line fit that will be explained in the following. It will be used to determine a function that converts a measured spectrum stored in units of channel to a an energy spectrum. Every line represents an energy deposition of electrons in the counting gas. Due to the limited energy resolution of the counter the single lines have a certain width σ_i and can be described by a gaussian function

$$f(x; a_i; \mu_i; \sigma_i) = a_i \cdot \exp(-\frac{(x-\phi_i)^2}{2\sigma_i^2}) \ . \tag{3.4.1}$$

Thereby a_i is the amplitude of the line i e.g. its relative intensity to the most intense line of the particular group peak and ϕ_i its theoretical position in the energy space. However, every group peak of the spectrum consists of a superposition of the individual gaussians described with equation 3.4.1 resulting in another function that can be specified by

$$F(x; A; \Phi; \Sigma) = A \cdot \sum_i \ a_i \cdot \exp(-\frac{(x-\alpha_i \cdot \Phi)^2}{2 \cdot (\beta_i \cdot \Sigma)^2}) \ . \tag{3.4.2}$$

The amplitude A of the entire group, the width Σ and, for our purpose most important its average position Φ are free parameters of the fit. To constrain and optimize the fit the relative deviations α_i and β_i have to be considered described by

$$\alpha_i = \frac{\phi_i}{\phi_{\mathrm{AP}}} \quad \text{and} \quad \beta_i = \frac{\sigma_i}{\sigma_{\mathrm{AP}}} \tag{3.4.3}$$

with the theoretical average position ϕ_{AP} in energy space and the average theoretical width σ_{AP} of the group peak. ϕ_i describes the theoretical energy and σ_i its width for each single line. With the equations 3.3.1 and 3.2.2 one can calculate ϕ_i and ϕ_{AP} for each of the group peaks. The β_i can be determined in the following way. One can assume that the energy resolution

$$\mathrm{R} = \frac{\sigma_i}{\sqrt{\phi_i}} \tag{3.4.4}$$

of one specific proportional counter at a certain high voltage and pressure of the counting gas is constant in the small energy range like the one of a single group peak [31]. If we further assume that in this range in energy space the pulse intensity is proportional to the one in the channel space the relation 3.4.4 holds there as well. Therefore

$$\beta_i = \sqrt{\alpha_i} \tag{3.4.5}$$

and it can be determined theoretically to use it in equation 3.4.2. Each group peak in the cerium and ^{55}Fe spectra was fit with the function $F(x; A; \Phi; \Sigma)$. Thereby the position of each group peak was identified in the channel space. This information together with the known energy position will be used to determine a calibration function.

3.4.1 Calibration with $XeCH_4$

The calibration was done with both x-ray sources, cerium and ^{55}Fe, one after another to assure that the outer conditions stayed constant and their energy depositions in the counting gas can equally be used for calibration. That means that the set-up and especially the high voltage are the same during both calibrations. The high voltage could have the strongest influence on the functionality of the energy scale. Since the high voltage is rather low in the measurements done in this work the low energy peaks of cerium with 0.3 keV and 1.1 keV are not resolvable in the channel spectrum and hence they cannot be used for calibration. The calibration was done with the peaks at 5.1 keV, 9.8 keV, 34.6 keV and 39.4 keV that are produced by the cerium x-ray source in xenon and with the

peak at 5.95 keV that is produced by the energy depositions of the ^{55}Fe decay. In the following the fit of each peak will be explained in more detail.

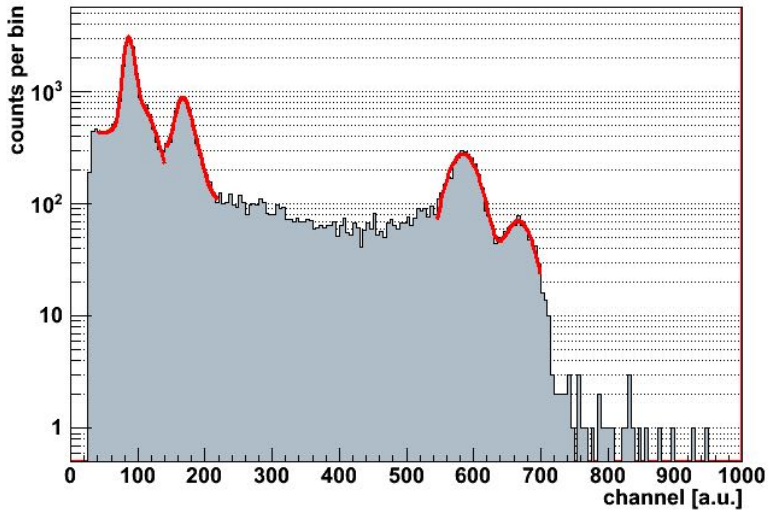

Figure 3.10: Channel spectrum of cerium x-rays in $XeCH_4$. Shown are fits to the peaks at energies of 5.1 keV, 9.8 keV, 34.6 keV and 39.4 keV.

Cerium at 5.1 keV Since this peak also contains energy depositions of the 6.5 keV iron peak in the same range one cannot fit them individually without any mutual overlap. In most cases one cannot even distinguish the iron peak from the 5.1 keV peak because the counter's energy resolution is not good enough and the 6.5 keV peak is suppressed. Moreover their relative intensities strongly depends on the irradiation geometry between x-ray source and counter that differs in every calibration. If the two peaks are not distinguishable one can fit them together with a fixed distance between both theoretical maxima by assuming that the energy scale is linear in this range. Doing so only the position of the 5.1 keV peak can be used for calibration. Since the relative amplitude of the cerium and iron peak are in general not known the amplitude of the latter is a free parameter in the fit.

Cerium at 9.8 keV This peak has no contribution from another group peak and so it can be fit most precisely in comparison with the other group peaks.

Cerium at 34.6 keVand 39.4 keV The relative distance between the maxima of these two peaks is great enough that they can be distinguish even if

the peaks themselves overlap and were not fit individually. This gives the possibility to fit both peaks together *without* fixing their relative distance. Doing so one gains two more calibration points. Fig. 3.10 shows a fit of the entire channel spectrum in $XeCH_4$.

Background models and systematic error estimation To describe the channel spectrum correctly and to improve the fit results one also has to consider the background and its potentially impact on the peak position. Different background models were fit to each group peak together with the multiple line fit since an explicit background description is not known. Thereby one can estimate the systematic error of the peak positions arising from a potentially background misinterpretation. In the following a model of a constant, a linear and an exponential decreasing background was assumed. It turned out that the peak positions barely depend on the chosen background model and hence that they are robust against the background model. The systematic error was estimated for every group peak by the standard deviation of peak positions varying the background model. Since a linear decreasing background seemed to reproduce the data best, its value was used for calibration. They systematic error was added quadratically to the error determined by the fit under the assumption of a linear decreasing background. The determined peak positions in channel space are stated in Table 3.3.

^{55}Fe at 5.95 keV The spectrum was recorded before and after each calibration run with cerium. The background was assumed to decrease linearly and it was fit together with the multiple line fit of ^{55}Fe as seen in Fig. 3.11a. To estimate a systematic error arising from the imprecise background knowledge the fit range was varied and thus different peak positions determined. The standard deviation of this positions was calculated and quadratically added to the error of the fit with the best fit result.

Results:

The final results of the entire $XeCH_4$ calibration are given in Table 3.3. The energy of each peak is plotted as a function of the obtained peak positions, presented in Fig. 3.11b. A polynomial of first and second degree was fit to these data. The obtained parameters are shown in Table 3.4. In [46] the same method of an energy calibration is applied by using cerium x-rays in xenon. Thereby a polynomial of second order describes the data best. However in the measure-

ments of [46] the high voltage of the set-up was higher than the one used in the measurements of this work. In the present example of an energy calibration with the parameters in Table 3.4 we obtain a $\chi^2/ndf = 27/3$ in the case of the linear fit and $\chi^2/ndf = 16/2$ in the case of the polynomial of second order. However this is just one example. During this work the calibration was done with several counters filled with $XeCH_4$. Generally no distinct preference was observed from the determined χ^2/ndf's by fitting a polynomial of first or second order to the data. Therefore we decided to chose the simpler model less parameters, the first degree polynomial, in the following to determine the calibration functions for counter filled with $XeCH_4$.

fit model	**5.10 keV**	**5.95 keV**	**9.76 keV**	**34.56 keV**	**30.43 keV**
constant	88.0 ± 0.1		168.6 ± 0.3	582.2 ± 0.6	667.9 ± 1.3
linear	87.5 ± 0.1	103.0 ± 2.3	169.2 ± 0.5	582.4 ± 0.6	666.0 ± 1.7
exponential	87.8 ± 0.1		169.8 ± 0.4	586.5 ± 0.8	666.4 ± 1.3
final result	87.5 ± 0.1	103.0 ± 2.3	169.2 ± 0.6	582.4 ± 1.5	666.0 ± 1.8

Table 3.3: Fit results for each group peak in $XeCH_4$ calibration in units if channel [CH]. A model of a constant, a linear and an exponential decreasing background was assumed and fit together with the multiple line fit to estimate a systematic error. The last row shows the positions determined in the channel spectrum that are used for calibration.

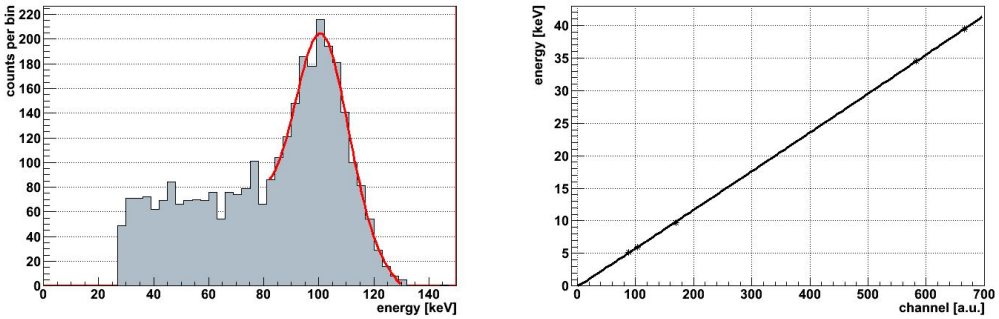

(a) ***(b)***

Figure 3.11: ***(a)*** Spectrum and fit of $XeCH_4$ radiated with ^{55}Fe x-ray source. ***(b)*** Polynomial of first and second degree fit to calibration data of Table 3.3.

parameters	$f(x) = p_0 + p_1 \cdot x[ch]$	$g(x) = p_0 + p_1 \cdot x[ch] + p_2 \cdot x[ch]^2$
p_0	$-1.93 \cdot 10^{-1}$	$-1.13 \cdot 10^{-1}$
Δp_0	$7.29 \cdot 10^{-4}$	$1.90 \cdot 10^{-3}$
p_1	$5.96 \cdot 10^{-2}$	$5.87 \cdot 10^{-2}$
Δp_1	$1.79 \cdot 10^{-6}$	$1.78 \cdot 10^{-5}$
p_2	-	$1.09 \cdot 10^{-6}$
Δp_2	-	$2.38 \cdot 10^{-8}$

Table 3.4: Parameters gained from fitting a polynomial of first and second degree to calibration data of Table 3.3.

3.4.2 Calibration with $ArCH_4$

As described in section 3.3.2 a calibration with cerium in $ArCH_4$ only is not possible. The high energetic cerium x-rays have a large range in argon and are not absorbed in the small active volume of the counter. For this reason a small amount of xenon gas was admixed that should serve as a target for these x-rays. They have a higher cross section to ionize xenon atoms than the argon atoms. The resulting electrons most likely depose their energy in argon as it is more abundant. The energy deposition of cerium x-rays in pure $ArCH_4$ was in the following regarded as background. Therefore a pure $ArCH_4$ spectrum was subtracted from spectra of $ArCH_4$ containing 2 % and 5 % xenon, respectively. This also allows the fit of the high energetic and less intense 34.6 keV peak. The pure $ArCH_4$ and xenon-containing spectrum were normalized to the same data taking time. The $ArCH_4$ spectrum was fit to spectrum of $ArCH_4$ containing a small amount of xenon, in the range where the continuum between converted and non-converted peaks is shaped equally in both spectra. The result of the so called difference spectrum can be seen in Fig. 3.12 in the example of the 2 % xenon admixture. In the range between channel 220 and 320 the spectra were overlaid resulting in fluctuations around zero in the same region in the difference spectrum. In Fig. 3.13 the difference spectrum is shown with respective errors of each bin. They include the error propagation arising from the subtraction. The multiple line fit was applied to this spectrum as in the case of $XeCH_4$.

Cerium at 5.1 keV A fit containing the superposition of the 5.1 keV group peak and the 6.5 keV peak originating from the excitation of the iron cathode was done with a fixed distance between the center of both peaks.

Cerium at 9.76 keV This peak has no contribution from another group peak and so it can be fit most precisely in comparison with the other group peaks.

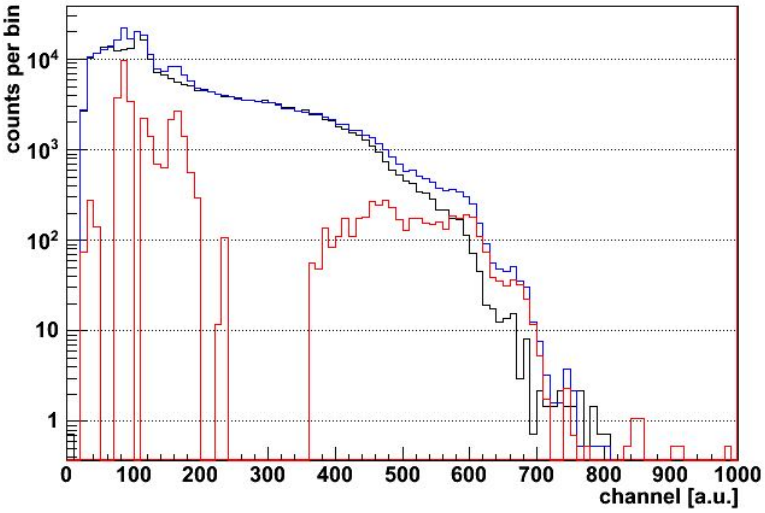

Figure 3.12: Spectra of cerium x-rays in pure $ArCH_4$ (black) and $ArCH_4$ with 2 % xenon (blue). The red spectrum shows the difference of both.

Cerium at 34.56 keV The intensity of the 39.4 keV was too low that a fit of this peak was possible. However the 34.6 keV peak was fit taking the superposition of the 39.4 keV peak into account.

^{55}Fe at 5.95 keV The systematic error was estimated by varying the fit range as in the case of $XeCH_4$. The multiple line fit of ^{55}Fe can be seen in Fig. 3.14.

Results:

Table 3.5 shows the results of the multiple line fit in the described case of an $ArCH_4$ spectrum with 2 % xenon admixture. Table 3.6 presents the parameters for a linear and quadratic function that was fit to the obtained results. In the case of the linear fit function we determine $\chi^2/ndf = 109/2$ and in the case of a quadratic function $\chi^2/ndf = 107/1$. As the calibration peaks have low intensities in comparison with the background, the fit of the $ArCH_4$ spectrum with 2 % xenon yields to rather high χ^2/ndf.

In the case of a 5 % xenon admixture the peaks become more distinguishable. The obtained peak positions are also shown in Table 3.5. In the case of fitting a polynomial of first order to the data $\chi^2/ndf = 22/2$ and by fitting a polynomial of second order we determine $\chi^2/ndf = 17/1$.

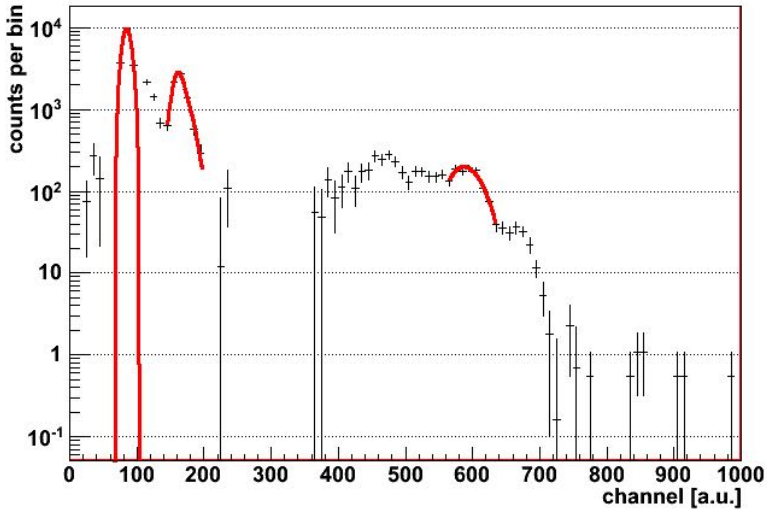

Figure 3.13: Difference spectrum with the corresponding errors . The three group peaks of 5.1 keV, 9.76 keV and 34.56 keV were fit.

In these two examples the linear fit describes the date better. The calibration was also done for other counters, always using $ArCH_4$ and a 5 % xenon admixture. As in the case of the calibration with $XeCH_4$ no clear preference was observed of describing the data either with a polynomial of first or second order. Therefore the counter filled with $ArCH_4$ and the xenon admixture were always calibrated by using a linear function.

The determined slopes of the 2 % and 5 % admixture agree within their error bars. This leads to the conclusion that small amounts of xenon atoms do not influence the main energy deposition of the calibration electrons in $ArCH_4$ and that the described method can be used for the calibration of $ArCH_4$. In the calibration of $ArCH_4$ we always used a 5 % xenon admixture in the following.

energy	**5.10 keV**	**5.95 keV**	**9.76 keV**	**34.56 keV**
2 % xenon	85.4 ± 0.2	102.8 ± 0.2	164.7 ± 0.6	580.7 ± 4.6
5 % xenon	85.8 ± 0.3	101.8 ± 0.2	165.5 ± 0.7	578.7 ± 4.8

Table 3.5: Fit results in units of channel [CH] for each group peak for $ArCH_4$ containing either 2 % or 5 % of xenon.

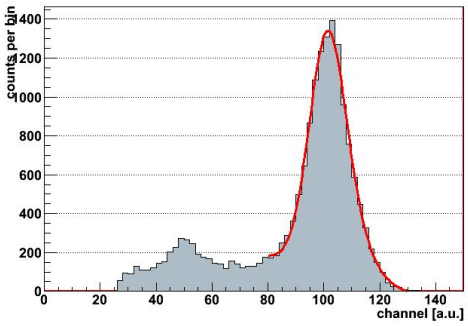

Figure 3.14: Spectrum of $ArCH_4$ containing 2 % xenon radiated with ^{55}Fe x-ray source.

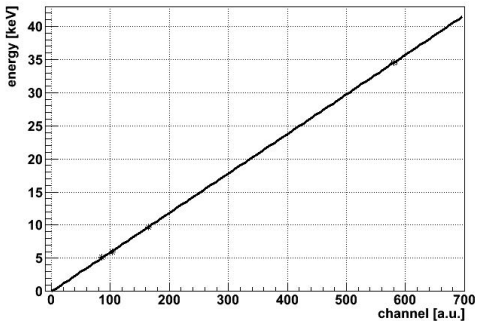

Figure 3.15: Polynom of first and second degree fit to the calibration data of $ArCH_4$.

parameters	$f(x) = p_0 + p_1 \cdot x[ch]$	$g(x) = p_0 + p_1 \cdot x[ch] + p_2 \cdot x[ch]^2$
p_0	$-7.88 \cdot 10^{-2}$	$-5.11 \cdot 10^{-2}$
Δp_0	$7.63 \cdot 10^{-4}$	$2.63 \cdot 10^{-3}$
p_1	$5.97 \cdot 10^{-2}$	$5.94 \cdot 10^{-2}$
Δp_1	$2.47 \cdot 10^{-6}$	$2.68 \cdot 10^{-5}$
p_2	-	$4.28 \cdot 10^{-7}$
Δp_2	-	$3.89 \cdot 10^{-8}$

Table 3.6: Parameters gained from fitting a polynomial of first and second degree to relation between channel and theoretical energy in the calibration of $ArCH_4$ with a 2 % admixture of xenon.

3.5 Systematic Errors

3.5.1 Parameterization of energy scale:

In the last section no clear preference was identified, for both counting gases, in using either a linear or quadratic function in the parameterization of the energy scale. We decided to use the linear parameterization as this is the simpler model with less parameters. However, this section should demonstrate the difference of both parameterizations. Fig. 3.16 displays spectra of a radon standard measurements by using either the counting gas $XeCH_4$ or $ArCH_4$. The black histogram indicates the spectrum calibrated with the linear function and the red histogram shows exactly the same spectrum calibrated with a quadratic function. At small energies the deviation of the histograms is small and increases towards higher energies. At high energies the discrepancy between both calibration functions is

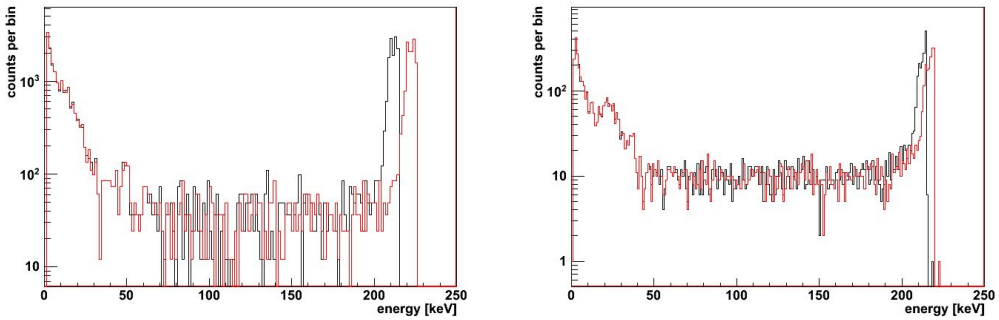

(a) *(b)*

Figure 3.16: Spectra of radon standard measurement in ***(a)*** $XeCH_4$ and ***(b)*** $ArCH_4$, with a linear (black) and quadratic (red) energy scale.

visible especially by regarding the overflow channel [2].

Table 3.7 shows for three different channels the relative deviation between the corresponding energies determined by using either the linear or quadratic calibration of the energy scale. This deviation is small up to energies of the most energetic cerium x-ray at $\sim 39\,\mathrm{keV}$. From this point on the energy scale can only be extrapolated since a calibration point at higher energies was not available. In the next chapter a comparison of background spectra are presented measured with both counting gases. The background spectra are presented till a range of 100 keV with a deviation of 0.9% and 1.78% in $ArCH_4$ and $XeCH_4$, respectively. In chapter 5 a lower energy threshold with the best sensitivity for ^{222}Rn is determined. The highest determined thresholds are in the range of 100 keV. The small deviation that could arise by using a quadratic calibration function instead of a linear calibration function can be omitted.

description	channel and energy	dev. in $XeCH_4$	dev. in $ArCH_4$
calibration limit	700 ($\sim 40\,\mathrm{keV}$)	0.1	0.17
range in chapter 3	1700 ($\sim 100\,\mathrm{keV}$)	1.78	0.9
overflow channel	3500 ($\sim 210\,\mathrm{keV}$)	5.09	2.28

Table 3.7: Deviation (in %) of energy values gained from quadratic calibration function relative to the one calculated with the linear calibration function. Deviations are given for both studied counting gases depending on the channel.

[2] High energetic events cause the amplifier to saturate and are counted in the so-called overflow channel

3.5.2 Influence of HV changes:

Small changes of the counter's high voltage can occur during a measurement. They could modify the calibration function. To study this potential modifications a counter filled with $XeCH_4$ was calibrated at different high voltages. The deviation of the slopes was estimated among the calibration function.
In a first calibration the initial channel (101.7 ± 0.4) was set as reference channel in the calibration with the 5.95 keV peak generated by the ^{55}Fe source. Afterward the counter was irradiated with cerium. With these two calibrations the reference calibration function was determined. Afterwards the calibration with these two sources was done with the three initial channels at channel (92.1 ± 0.4), (104.0 ± 1.1) and (126.8 ± 0.6). The first two setting should simulate normal HV changes as they can occur during the measurements. The channel (126.8 ± 0.6) presents a rather extreme shift in the high voltage. The relative slope deviation D_{slope} between the calibration function using $(101.7 \pm 0.4\ )$ as reference channel and the calibration functions bases on another initial channels was determined. They are shown in Table 3.8. The deviation D_{slope} and hence the calibration function is very sensitive to voltage changes. If the high voltage changes too much during a measurement it must be discarded. In general the peak position of the ^{55}Fe calibration is compared before and after a measurement or even during measurements to assure that the calibration stays constant over time.

initial channel	$D_{channel}$ [%]	D_{slope} [%]
101.7 ± 0.4	-	-
92.1 ± 0.4	9.9	6.7
104.0 ± 1.1	3.5	2.7
126.8 ± 0.6	25.3	19.9

Table 3.8: Relative channel deviation $D_{channel}$ and relative slope deviation D_{slope} for different high voltages relative to channel (101.7 ± 0.4).

3.5.3 Deviation among different counters and set-ups:

Since the calibration method described in section 3.4.2 for $ArCH_4$ was developed and tested at the end of this work, it was not possible to calibrate individually every measurement using this counting gas. Measurements with $XeCH_4$, however, could all be calibrated individually. In order to calibrate also the measurements in pure $ArCH_4$ without the admixture of a small amount of xenon gas, we transferred a calibration function determined with another counter to these measurements. In doing so, several systematic errors could occur. We consider two cases in the

following:

case 1) The calibration of counter A was done for a particular measurement and is transferred to another measurement, without calibration, with the same counter A

case 2) The calibration of counter A was done for a particular measurement and was transferred to another measurement with counter B as no calibration of B is existing

For case 1) we estimate a systematic error of 2.5 %.This was the maximal slope deviation that was found, however, for different $XeCH_4$ calibrations in subsequent measurements with one counter. The error is transferred to measurements done with $ArCH_4$ since there was at maximum one calibration function available for a particular counter using this counting gas and hence no comparison to another measurement possible. The systematic error in case 1) could arise from pressure differences, HV changes and the use of different pre-amplifiers.

For case 2) we estimate 8.4 %. This was the maximal slope deviation among calibration function of different counters determined in $ArCH_4$. The systematic error in case 2) could arising from the same conditions as in case 1). Furthermore differences among counters like slightly different electric field can cause this deviation.

The described error estimation is true for one particular set-up. The background measurements were done at MPIK, Heidelberg and at LNGS, Italy. By the comparison of measurements done with the same counting gas and counter but different set-ups a maximal slope deviation of 17.17 % was found. This cannot be explained by the usual pressure deviations of the counting gas among different measurements. An explanation could be that the high voltage of the two set-ups is unequal. The influence of high voltage changes are shown in section 3.5.2. In cases were a calibration function for one particular counter was determined at e.g. LNGS but not at for the set-up at MPIK, the calibration function from another counter at the same set-up at MPIK was preferred. The error estimated in case 2) is relevant for these measurements.

In section 3.5.2 we saw a maximal slope's deviation of 6.7 % arising from normal HV changes, as they can occur during measurements. Combined with the

error for measurement of case 1) this results in an overall systematic error of 7.2 %. Thereby the error due to HV changes was quadratically added to the one of case 1). In the same manner the overall systematic error of 10.7 % for case 2) was determined.

3.6 Conclusion

In chapter 3 the calibration of proportional counters filled either with the counting gas $ArCH_4$ or $XeCH_4$ is performed. This is necessary for comparing spectra measured with these two counting gases, as it will be done in the subsequent chapters 4 and 5. Cerium is usually used as calibration source in the case of $XeCH_4$. It induces *several* energy depositions in the counting gas and allows an energy calibration in a range up to $\sim 39\,\mathrm{keV}$. Thereby the energy scale's linearity can be examined. In measurements with $ArCH_4$ a ^{55}Fe source is usually used that emits x-rays at an average energy of $\sim 6\,\mathrm{keV}$ inducing a *single* peak that is used for calibration. In order to improve the energy calibration using $ArCH_4$ a new calibration method has been developed and successfully tested.

Chapter 4

Background energy spectra of proportional counters

In this chapter, the energy spectra of background measurements of proportional counters are presented. Background events are detected without sample and despite a particular shielding. The spectra were scaled to the arbitrary duration of 10 days to allow a better comparison whereas the real taking time was in all cases much longer. The background spectra were measured with two different counting gases, $ArCH_4$ and $XeCH_4$, in combination with three different shieldings. We describe the background sources that contribute for each of these combinations.

4.1 Overview on shieldings and energy spectra

During measurement the counter is always mounted in a lead holder, surrounded by a copper housing. The copper housing also contains the pre-amplifier. In addition, one of the following shielding was applied:

Above Ground (AG): the measurements were done in a laboratory above ground at MPIK in Heidelberg using lead bricks with a total thickness of $5 - 10\,\mathrm{cm}$ for shielding. A picture of this shielding is shown in Fig. 4.1a.

Gran Sasso (GS): the measurements were done in the underground laboratory at Gran Sasso at a depth of 3800 m.w.e.[22]. An equivalent shielding as above ground was additionally used.

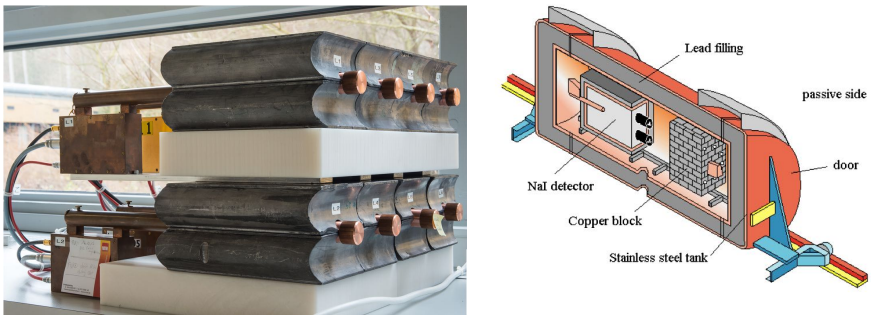

(a) *(b)*

Figure 4.1: ***(a)*** The counter is always placed into a copper housing during measurement. This housing is in turn mounted into bricks of lead. ***(b)*** Lead shielding, surrounded by a stainless steel container. The counters are mounted in a copper block during measurement. The NaI detector was not used in this study.

Lead Tank (LT): another counting system is available in the same underground laboratory at Gran Sasso. During the measurement the counters are mounted in a copper block. Depending on the position of the counter the shield thickness is $5 - 50\,\text{cm}$. This block has a 4π lead coverage as it is placed in a lead container, the so called "tank", that has a housing made out of stainless steel. A picture of the tank is shown in Fig. 4.1b. The tank has a wall thickness of about $\sim 10\,\text{cm}$. It is constantly flushed with boil-off nitrogen to suppress ambient air with its comparably high concentration of environmental radioactive radon.

The background spectra were recorded with both the counting gases $ArCH_4$ and $XeCH_4$ for each shielding, labeled additionally with "Ar" and "Xe", respectively. The $ArCH_4$ spectra were calibrated by using the method developed in chapter 3 and assuming the systematic errors explained in 3.5, if no individual calibration was possible. These errors for each counter and measurement are shown in Table.4.1. They do not arise for the $XeCH_4$ spectra since they could be all calibrated individually. The energy spectra are shown in Fig. 4.2 - 4.5 for the four counters C24, C30, C16 and C35, respectively. The solid lines represent the spectra of $ArCH_4$ whereas the dashed lines show the one of $XeCH_4$. The colors indicated the used shielding, whereby blue stands for "above ground", red for "Gran Sasso" and black for "lead tank".

Counter	HD	GS	LT
C24	-	7.2	individually calibrated
C30	10.7	10.7	no measurement
C16	10.7	7.2	individually calibrated
C35	10.7	7.2	individually calibrated

Table 4.1: Systematic error on background energy spectrum (in %) for each counter and shielding using $ArCH_4$ as counting gas. They do not arise for measurements with $XeCH_4$.

One principle difference of the counting gases $ArCH_4$ and $XeCH_4$ is their unequal stopping power. The stopping power in xenon is higher than in argon which results in turn in a shorter absorption length for particles. Particles with the same energy can deposit more of it in xenon than in argon on the same track length. This is relevant in the following as the active volume of the proportional counter has a limited size. The stopping power of both gases is not sufficiently high, that high energetic particles are completely absorbed. For example the maximal deposit energy for a high energetic electron on a covered track of 3 cm (which corresponds to the typical counter's length) is ca. 50 keV in $ArCH_4$ [39]. The maximal deposit energy in xenon is larger for the same high energetic electron. Consequently the spectra of $XeCH_4$ are shifted towards higher energies in comparison with the ones of $ArCH_4$. This effect can especially be seen for the spectra recorded above ground (blue lines), as there are many high energetic background particles abundant. In the next section we will describe the background contributions in more detail for each of the applied shielding.

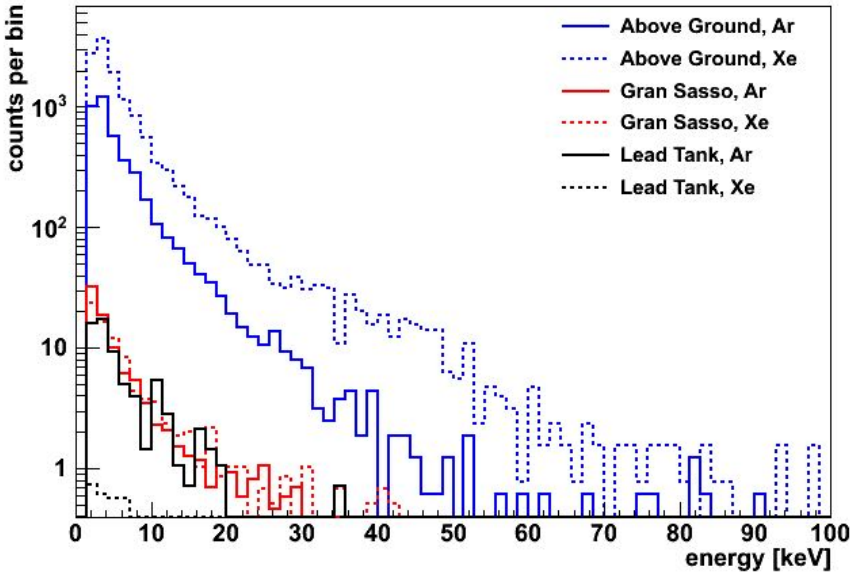

Figure 4.2: Background energy spectrum of counter C24 for different shieldings and counting gases.

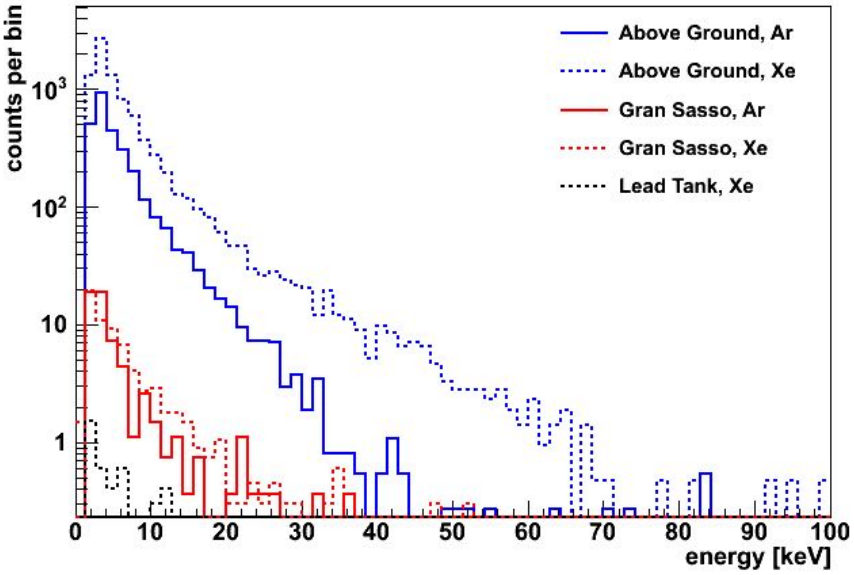

Figure 4.3: Background energy spectrum of counter C30 for different shieldings and counting gases.

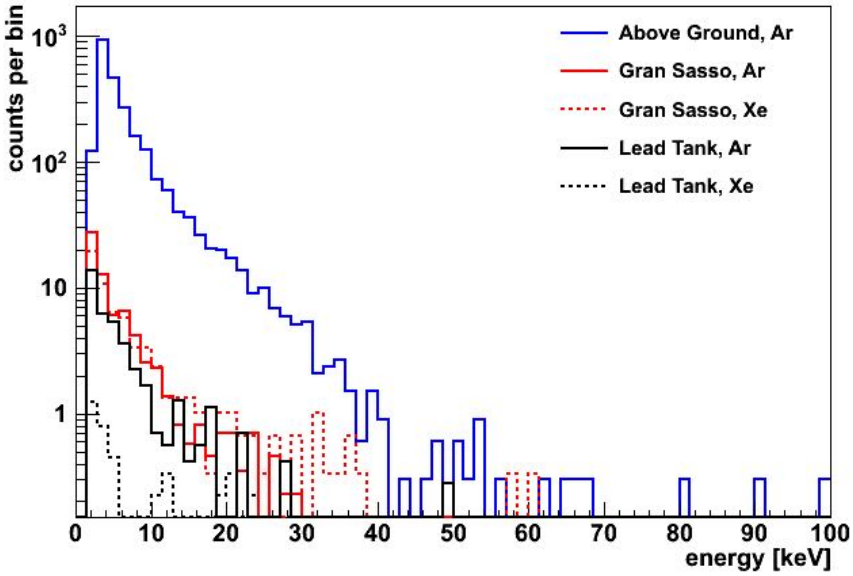

Figure 4.4: Background energy spectrum of counter C16 for different shieldings and counting gases.

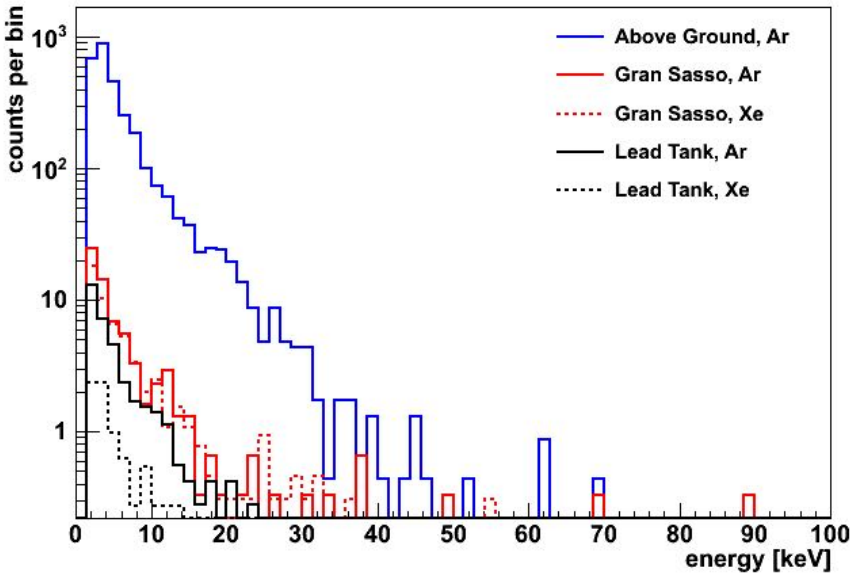

Figure 4.5: Background energy spectrum of counter C35 for different shieldings and counting gases.

4.2 Background Contributions

Different radiation sources could contribute to the background measured with the proportional counters. Some of these contributions originate from external radiation that can be reduced or even undesirably enhanced by the different shieldings. Independent from any shielding, there are intrinsic background sources. They can be either induced by impurities of the counter's material or as a consequence of the ^{222}Rn measurements.

Intrinsic background

The decay chain of ^{222}Rn includes the long-lived progeny ^{210}Pb. Once created it could get permanently attached to the walls and the anode wire of the counter. With a rather long live-time of 22.3 years the decay of this isotope can always contribute to the activity of subsequent measurements. The energy spectrum of the β-particles emitted in the decay has an energy end-point at about 60 keV. This kind of intrinsic background cannot be avoided but minimized by measuring high activity samples shortly. The expected background enhancement is 0.02 events/day per mBq of ^{222}Rn [39].

The intrinsic background due to impurities of the counter's material is small as the proportional counter were developed for the GALLEX experiment that required an extremely low background. The values of the intrinsic background are listed in [24]. The main contribution arises from the uranium in the iron cathode with less than 0.3 events/day.

A significant difference of the event rate in $ArCH_4$ and $XeCH_4$ is conspicuous if the counters are placed inside the lead tank at Gran Sasso. Thereby they are most shielded from ambient radiation, especially γ-rays, in comparison with the other shieldings that were used in this study. The event rate for measurements with $ArCH_4$ as counting gas are much higher than with $XeCH_4$. The supposition of an intrinsic contamination with the radioactive ^{39}Ar in $ArCH_4$ was discarded. As measured in [49] the ratio of g(^{39}Ar)/g($^{\mathrm{nat}}$Ar) is $(8.0 \pm 0.6) \cdot 10^{-16}$. With a typical mass of ca. 10 μg of Ar in the counter's active volume the amount of ^{39}Ar is completely negligible. The higher background rate in $ArCH_4$ compared to the one in $XeCH_4$ is not understood.

Lead shield

Due to the high atomic number lead is one of the best shielding materials. However there is one disadvantage in using it, namely its intrinsic contamination with the radioactive ^{210}Pb. It is the only source of its intrinsic radioactivity. The β particles in the ^{210}Bi decay can produce bremsstrahlung and x-rays since they have an energy of ca. 1.2 MeV [49]. The continuum of the bremsstrahlung has a maximum at 170 keV and the maximal x-ray energy is 87.4 keV [24]. If this radiation is produced close to the counter, the self-shielding of the lead cannot stop it from entering its active volume. Since the proportional counters are always shielded with lead during the measurements its described contribution is existing in addition to the intrinsic background. Note that this contribution arises mainly from the lead bricks and the lead tank and not from the lead frame the counter is mounted in. For this frame especially pure lead was used [58].

Environmental radiation

The γ radiation generated by environmental radioactivity almost exclusively originates from γ-rays of the uranium and thorium decay series and of the ^{40}K decay. The most energetic naturally occuring γ line from ^{208}Tl has an energy of 2.6 MeV [55]. γ radiation due to the decay of ^{222}Rn is suppressed inside the lead tank as this cavity is always flushed with boil-off nitrogen. This could be an explanation for the slightly lower event rate of $ArCH_4$ spectra recorded inside the tank in comparison with the one outside (solid red and black lines). However it cannot explain the mentioned significant lower event rate of the $XeCH_4$.

Muons

Muons are produced in the decay chain of charged mesons in the atmosphere's showers as a result of the interaction of primary cosmic rays with the air. They mainly lose their energy to ionization on their way through the atmosphere resulting in an average energy of about 4 GeV at sea level [14]. They are also the most numerous charged particle at sea level that originated from cosmic rays. Less intense are neutrons, electrons, protons and pions in decreasing order. Besides muons and neutrons, all of these particles are already absorbed by overburden such as building ceilings [15] and they can also easily penetrate the lead shield. At the overground laboratory in Heidelberg muons and neutrons induced by cosmic rays make up the biggest contribution to the background events. The muons can additionally generate electromagnetic showers in the lead shield. The produced

particles and γ-rays could be detected by the counter. In contrast to charged particles γ-rays do not always lead to an ionization of the counting gas but can rather escape from the active volume without inducing a signal. The probability of being stopped is higher in $XeCH_4$ than in $ArCH_4$. This could be an explanation for the different event rate in both counting gases [58]. The effect is most dominant above ground since the high muon flux generates γ-rays in the lead shield. At Gran Sasso the muon flux is reduced by a factor of 10^6 with respect to the surface [22]. The remaining γ-rays originate mainly from environmental radiation. For muons reaching great depths bremsstrahlung, direct electron-positron pair production and electromagnetic interaction with nuclei are important. In these radiative processes energy is lost in showers along the muon path [20]. For measurements done at Gran Sasso the contribution from muons themselves is negligible. More important are their mentioned secondary particles, especially neutrons.

Neutrons

Above ground neutrons from cosmic radiation make up the largest contribution of neutron induced background. This neutron flux is reduced by a factor of 10^3 in the underground laboratory at Gran Sasso with respect to the surface [22]. Other processes account for the main neutron background in these depths. They can be produced by subsequent (α,n) reactions after an α-decay from environmental radiation e.g. from the decay of ^{210}Po within the lead shield. Moreover they are produced in the process of spontaneous fission, whereas ^{238}U is the most important source [33]. In the underground laboratory at Gran Sasso these neutrons can contribute to the background in the case of using lead bricks. Neutrons can interact with the counter material and counting gas through nuclear recoil or they can produce radioactive nuclides within the lead or the detector. Moreover they can generate γ radiation by inelastic scattering or radiative capture [24]. Inside the tank, their contribution is small in comparison with the intrinsic background of the proportional counter [24] [58].

4.3 Counting Rates

For completeness we also state the counting rates for each background measurement. Fig. 4.6 presents the number of counts that are measured at one day with a lower threshold at channel 800 (about 50 keV)) for all measurements. The exact values are given in Table 4.2 in the column R_{cut}. For measurements done at MPIK the counting rates in $ArCH_4$ and $XeCH_4$ are different due to the described effect of unequal stopping power in xenon and argon. The spectra of $XeCH_4$ are shifted to higher energies in comparison to $ArCH_4$ and consequently more events are detected above the energy threshold of 50 keV. This effect is not observed for measurements in the underground laboratory at Gran Sasso neither inside nor outside the lead tank. The counting rates above the mentioned energy cut are equal for both counting gases and shieldings as there are less high energetic particles abundant. Fig. 4.6a shows the *total* number of counts measured at one day, for the two different shieldings at Gran Sasso and both counting gases. Thereby no additional energy threshold is applied[1]. The rates are just given for the counter C30, C16 and C35 for demonstration since the values for counter C24 are significantly higher and probably outliers. The Fig. 4.6b shows that the counting rate is independent on the used counting gas at low energies outside the lead tank. However for measurements inside the lead tank the counting rate in $ArCH_4$ is significantly higher than in $XeCH_4$. The values for the total counting rates are given in Table 4.2 as R_{tot}. Moreover the fraction F of counting rates are shown relative to the rate R_{tot} above ground using $ArCH_4$.

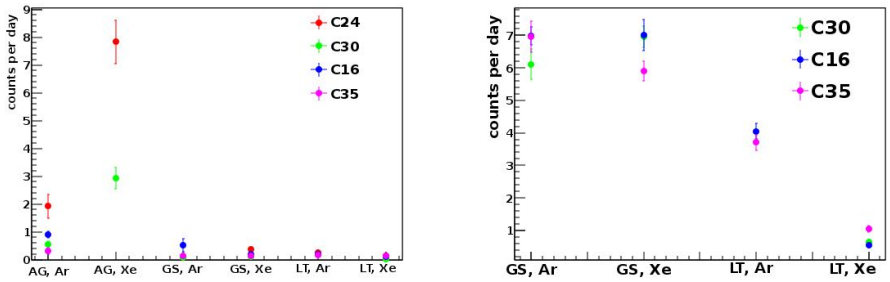

(a) *(b)*

Figure 4.6: ***(a)*** Counting rates lower threshold at about 50 keV. They are shown for the counters C24, C30, C16 and C35, respectively. ***(b)*** Counting rates without any energy threshold. They are shown for the counters C30, C16 and C35, respectively.

[1]The DAQ system sets always an lower threshold at a few keV to reduce electronic noise

shielding, gas	fraction F [%]	R_{tot} [cpd]	R_{cut} [cpd]
AG, $ArCH_4$	100	6995 ± 70	1.9 ± 0.4
AG, $XeCH_4$	241 ± 3	16885 ± 114	8 ± 1
GS, $ArCH_4$	2.6 ± 0.1	186 ± 5	0.07 ± 0.03
GS, $XeCH_4$	1.3 ± 0.1	94 ± 4	0.4 ± 0.1
LT, $ArCH_4$	1.0 ± 0.1	73 ± 5	0.3 ± 0.1
LT, $XeCH_4$	0.08 ± 0.01	6 ± 1	0.12 ± 0.03

shielding, gas	fraction F [%]	R_{tot} [cpd]	R_{cut} [cpd]
AG, $ArCH_4$	100	479 ± 4	0.5 ± 0.1
AG, $XeCH_4$	249 ± 2	1193 ± 7	2.9 ± 0.4
GS, $ArCH_4$	1.3 ± 0.1	6 ± 1	0.07 ± 0.05
GS, $XeCH_4$	1.5 ± 0.1	7.0 ± 0.3	0.10 ± 0.04
LT, $XeCH_4$	0.14 ± 0.02	0.7 ± 0.1	0.03 ± 0.02

shielding, gas	fraction F [%]	R_{tot} [cpd]	R_{cut} [cpd]
AG, $ArCH_4$	100	569 ± 4	0.9 ± 0.1
GS, $ArCH_4$	1.2 ± 0.1	7.0 ± 0.3	0.5 ± 0.2
GS, $XeCH_4$	1.2 ± 0.1	7.0 ± 0.5	0.20 ± 0.08
LT, $ArCH_4$	0.71 ± 0.04	4.0 ± 0.2	0.2 ± 0.1
LT, $XeCH_4$	0.09 ± 0.01	0.5 ± 0.1	0.10 ± 0.03

shielding, gas	fraction F [%]	R_{tot} [cpd]	R_{cut} [cpd]
AG, $ArCH_4$	100	500 ± 5	0.3 ± 0.1
GS, $ArCH_4$	1.4 ± 0.1	7.0 ± 0.5	0.1 ± 0.1
GS, $XeCH_4$	1.2 ± 0.1	5.9 ± 0.3	0.12 ± 0.04
LT, $ArCH_4$	0.7 ± 0.1	3.7 ± 0.2	0.2 ± 0.1
LT, $XeCH_4$	0.21 ± 0.02	1.0 ± 0.1	0.14 ± 0.04

Table 4.2: Counter C24,C30,C16,C35. Presented are the fractions F relative to the rate of the measurements "above ground", the rates R_{tot}, without any energy cut and the rate R_{cut} with a energy cut at ca. 50 keV for different shieldings and counting gases. Rates are given in counts per day.

4.4 Conclusion

Energy spectra of background measurements were presented for four different proportional counters. The measurement were done in all combinations using two different counting gases and three shieldings. As counting gas either $ArCH_4$ or $XeCH_4$ was used. A copper housing with a lead frame as shielding was common for all measurements. At a laboratory above ground at MPIK lead bricks were used in addition. The other two shielding options were an equally set-up as above ground and a completely enclosing lead tank constantly flushed with boil-off nitrogen. Both of them are placed in an underground laboratory at Gran Sasso with depth of 3800 m.w.e. The main background contribution above ground are neutrons and muons. Muons can also produce showers in the lead bricks whereby secondary particles can enter the active volume of the counter. At Gran Sasso mainly γ-radiation of environmental radioactivity and neutrons from (α,n) reactions or fission generate the background events. Inside the lead tank the contribution of the γ and neutron radiation is reduced and intrinsic background forms the main contribution.
In the next chapter these background spectra are used to optimize the sensitivity for the different combinations of counting gas and shielding.

Chapter 5

Sensitivity optimization

$ArCH_4$ and $XeCH_4$ are two common counting gases used with proportional counters to detected ionizing particles . In the section we want to study if one of these counting gases is more suitable in the detection of ^{222}Rn decays for a further a improvement of the ^{222}Rn emanation measurements. Moreover we want to test this related to different shieldings that serve for the protection of the proportional counters from ambient radiation. More information on the measured background spectra and applied shieldings can be found in chapter 4.

5.1 General Method

In the following study the *sensitivity* S is determined for different lower energy thresholds i of the measured spectra. This quantity, defined as

$$\mathrm{S}_i = \frac{\tilde{\mathrm{N}}_i}{\epsilon_{\mathrm{c},i} \cdot \mathrm{t}}\,, \tag{5.1.1}$$

expresses the ratio of the *decision threshold* $\tilde{\mathrm{N}}$ and the *counter efficiency* ϵ_c, whereby t is the measurement time. The decision threshold describes the minimum measurable number of counts that can be distinguished from background events with a certain probability. The lower the decision threshold the lower is the required number of counts that can still be classified as such and not misidentified as background. This makes sure that also low-activity samples are measurable. The efficiency characterizes the ratio of detected number of counts to the number of radon atoms. A high efficiency provides better statistics and hence a more precise measurement of the sample's activity. The determination of the decision threshold and the efficiency is explained in the subsequent sections. We want

to identify the *minimum* of their ratio with the corresponding energy threshold i. At this minimum the sensitivity is optimized. For linguistic simplification we describe the optimized sensitivity as *maximal* sensitivity even though we want to determine the minimum of S_i. The results on the sensitivity are presented for different counters and diverse combinations of counting gas and applied shielding.

5.1.1 Efficiency

As described at the end of section 2.2 the efficiency $\epsilon_{c,i}$ above an energy threshold i can be deduced as

$$\epsilon_{c,i} = \frac{N_{m,i} \cdot \lambda}{\epsilon_{fill} \cdot \epsilon_{yield} \cdot A_0 \cdot e^{-\lambda \cdot t_1} \cdot (e^{-\lambda \cdot t_1} - e^{-\lambda \cdot t_2})} . \tag{5.1.2}$$

Thereby $N_{m,i}$ are the number of counts measured in a time interval $[t_1, t_2]$ above the particular energy threshold. The decay constant of ^{222}Rn is specified by λ. ϵ_{fill} and ϵ_{yield} stand for the filling efficiency and the yield efficiency, respectively. Their exact evaluation is described in [LIN]. A_0 is the initial activity of the sample before extraction when the saturation equilibrium is reached. The data evaluation is designed to determine A_0 with the premise of an exact knowledge of ϵ_c. In order to determine ϵ_c one measures a sample of known ^{222}Rn activity $A_0 = A_{ST}$, referred to standard.

Standard production

In order to measure a reference activity a liquid standard was used. It is based on a ^{226}Ra solution with known mass/activity ratio that was provided by the PTB[1]. By admeasure a small mass fraction a standard with an activity of (217.3 ± 5.5) mBq was produced. The ^{226}Ra solution was diluted with $BaCl_2$. The liquid is contained in a glass vessel to collect the emanating ^{222}Rn atoms.

Energy spectrum of ^{222}Rn standard

Fig. 5.1 shows the energy spectrum of a ^{222}Rn standard for both counting gases, $ArCH_4$ (red lines) and $XeCH_4$ (blue lines). Mainly the comparable short-lived daughter isotopes of ^{222}Rn contribute to the signal. These are: ^{218}Po, ^{214}Pb, ^{214}Bi and ^{214}Po. The α-decays in the decay chain of ^{222}Rn possess energies between

[1]The abbreviation PTB stands for "Physikalische Technische Bundesanstalt": http://www.ptb.de/index_en.html

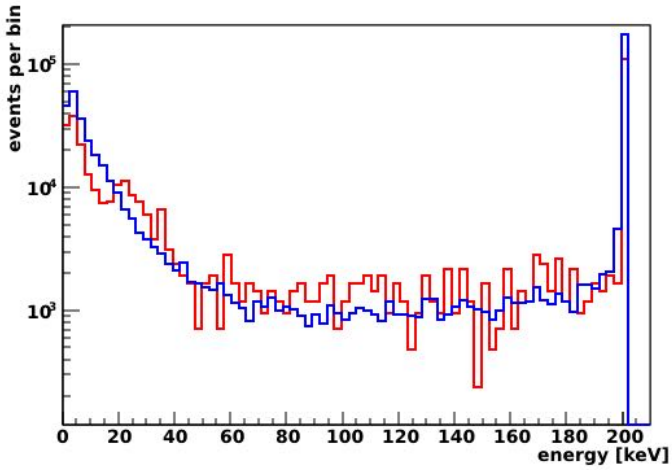

Figure 5.1: Energy spectrum of a standard activity in $ArCH_4$ (red lines) and $XeCH_4$ (blue lines).

$(5.5 - 7.7)\,\mathrm{MeV}$. They are fully adsorbed in the sensitive volume and cause the amplifiers to saturate. Any energy resolution is lost and the events are recorded in the overflow channel. The electrons of the β-decays have larger ranges as the α-particles. Hence the amount of deposited energy is lower. While the maximum electron's energy of a β-decay is 1.8 MeV their deposited energy is smaller than $\sim 50\,\mathrm{keV}$ due to the limited size of the active volume [39]. This is visible as a decrease of the event rate at small energies.

Efficiency's time evolution

As already mentioned ϵ_c describes the ratio of detected number of counts to the number of radon atoms. The number of detected counts arises from the α-decay of the ^{222}Rn atoms but also from successive decays of the ^{222}Rn daughters. The main contribution emerges from the decay chain until the long-lived isotope ^{210}Pb is attained:

$$^{222}\mathrm{Rn} \xrightarrow[\alpha]{3.8\ \mathrm{days}} {}^{218}\mathrm{Po} \xrightarrow[\alpha]{3.04\ \mathrm{min}} {}^{214}\mathrm{Pb} \xrightarrow[\beta]{26.9\ \mathrm{min}} {}^{214}\mathrm{Bi} \xrightarrow[\beta]{19.7\ \mathrm{min}} {}^{214}\mathrm{Po} \xrightarrow[\alpha]{2\cdot 10^{-4}\,\mathrm{s}} {}^{210}\mathrm{Pb} \tag{5.1.3}$$

The counter efficiency ϵ_c is constant over time if the production rates of these daughter isotopes are in equilibrium. However this takes a certain time period Δt depending on the half-lives of the daughter isotopes. This time period is referred to "rising phase". In this phase ϵ_c increases as more and more decays within the ^{222}Rn decay chain can contribute to the signal. The blue curve in

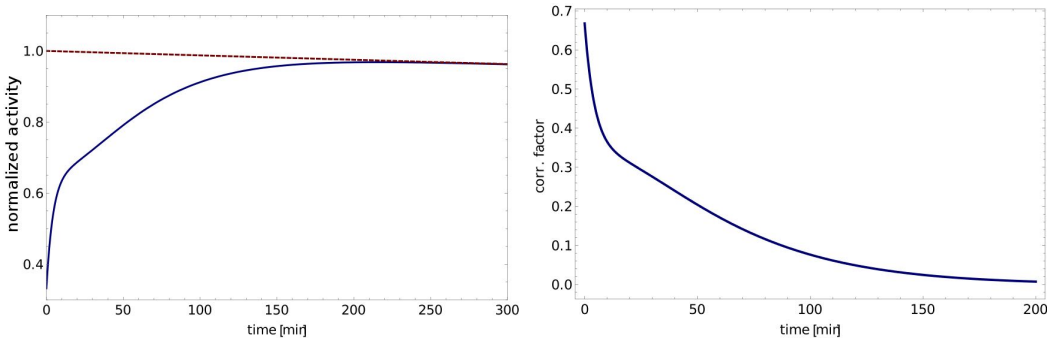

(a) *(b)*

Figure 5.2: ***(a)*** Red curve: activity A_{decay} showing radioactive decay of a sample. Blue curve: activity A_{sample} including the radioactive decay and the rise phase of the activity. ***(b)*** Time evolution of correction factor ϵ_{rise}. Figure courtesy of Stefan Brünner.

Fig. 5.7a shows the calculated time evolution of an activity A_{sample}. Thereby only the α-decays in the decay chain of Eq.5.1.3 generate the signal. The β-particles are neglected. The formula of the time evolution is given in Appendix A. A_{sample} considers the radioactive decay of the sample as well as the rising phase. From Fig. 5.7a we can see that the activity is increasing at the beginning due to the increasing contribution of ^{222}Rn daughters in the signal. If the production rates of these daughter isotopes are in equilibrium the decay of the sample, that is always present, becomes visible. Also presented as a red curve is the time evolution of an activity A_{decay} that considers only the radioactive decay. The shown activities are calculated relatively to the initial activity A_{fill} that is normalized to 1. It deflects the activity at time t_{fill} when the counter is filled. From this moment on the ^{222}Rn atoms decay within the active volume and trigger the successive decay of the daughter isotopes and the rising phase. In general we have to correct for the initial increase of ϵ_c with a correction factor ϵ_{rise}, given by

$$\epsilon_{rise} = \frac{A_{sample}}{A_{decay}}. \tag{5.1.4}$$

The time evolution of ϵ_{rise} is shown in Fig.5.7b. The correction is included in the data evaluation with our data base. In this work we used another approach. Only data recorded after a time period Δt, starting from t_{fill}, when the deviation of A_{decay} and A_{sample} becomes negligible is used in the data evaluation. After this time Eq. 5.1.2 holds and ϵ_c is considered to be constant. Assuming that always

50 % of the α-decays are detected[2] the deviation is $< 1\,\%$ after a time period of $\Delta t_{1\%} = 188\,\text{min}$. In the subsequent evaluation of ϵ_c only measurements of a standard activity were used whose measurement periods start after $\Delta t_{1\%}$.

Decrease of standard's activity

An decrease of the standard activity over time was observed. During every extraction not only the emanated ^{222}Rn atoms are flushed out of the vessel but also a small fraction of evaporated solution. Consequently the liquid level decreases and $BaCl_2$ molecules could stay attached to the walls that were previously covered by the solution. Thereby they could enclose ^{226}Ra atoms. In the decay of ^{226}Ra the produced ^{222}Rn atom gets a recoil energy of 85 keV. If this energy is not sufficiently high the enclosed ^{222}Rn atom is stuck in the $BaCl_2$ layer and cannot escape anymore. In subsequent measurements the ^{222}Rn atoms could not get extracted which causes an apparently smaller ^{222}Rn activity [31]. The described effect is reversible by adding H_20 that could resolves the ^{226}Ra attached to the wall.

The efficiency ϵ_c is also an indication of the standard's activity stability. For the recent data evaluation an energy threshold of about 50 keV (channel 800) is applied with an efficiency of $\epsilon_c^{ref} = (1.47 \pm 0.06)\%$. It is the average result of several measurements using $ArCH_4$ as counting gas [59]. The efficiency for the same energy threshold and counting gas was measured to be $\epsilon_c^{new} = (1.50 \pm 0.07)\%$ with a freshly produced standard. It agrees with ϵ_c^{ref}. We observed an decrease of the efficiency after several measurements of the standard. The very same decline was observed for measurements using $XeCH_4$ as counting gas. The ratio of ϵ^{new} and the decreased efficiency is $R = (1.2 \pm 0.1)$. Since only a measurement of the already decreased standard activity was available with $XeCH_4$, the determined efficiencies $\epsilon_{c,i}^{Xe}$ were correct by the factor R. Thereby the uncertainty on $\epsilon_{c,i}^{Xe}$ increases which will be considered in this study by a modification of the general sensitivity definition. This should ensure that the determined sensitivities in $XeCH_4$ and $ArCH_4$ are still comparable.

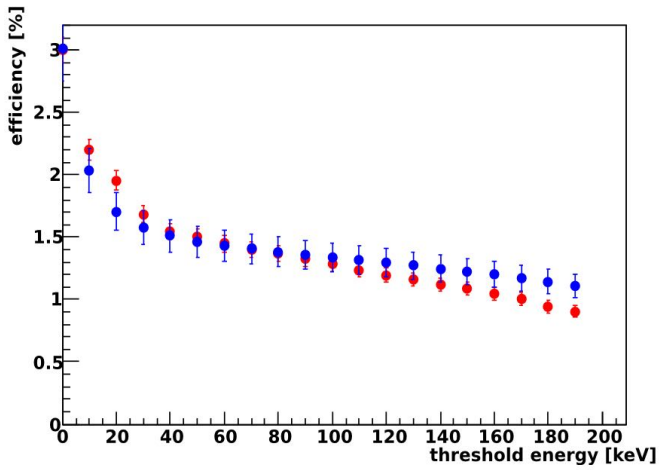

Figure 5.3: $\epsilon_{\mathrm{c,i}}$ for a standard activity measured in $ArCH_4$ (red) and $XeCH_4$ (blue).

Efficiencies in $ArCH_4$ and $XeCH_4$

The efficiencies $\epsilon_{\mathrm{c},i}$ were determined for the counting gases $ArCH_4$ and $XeCH_4$ using Equation 5.1.2. The applied energy thresholds i start at 0 keV (including all detected counts), are divided in steps of 10 keV and end at a maximum threshold of 190 keV. Events $N_{\mathrm{m},i}$ having energies above a certain energy threshold are considered for the particular $\epsilon_{\mathrm{c,i}}$. Only counts that were measured after the time period $\Delta t_{1\%}$ were considered (see section "Efficiency's time evolution"). In addition, the $\epsilon^{\mathrm{Xe}}_{\mathrm{c},i}$ for $XeCH_4$ were scaled by a factor of $R = (1.2 \pm 0.1)$ that accounts for the decreased standard activity (see section "Decrease of standard's activity"). The described efficiencies for $ArCH_4$ (red dots) and $XeCH_4$ (blue dots) are shown in Fig.5.3. As $N_{\mathrm{m},i}$ decreases for higher energy thresholds, also $\epsilon_{\mathrm{c,i}}$ is decreasing. The efficiency in $XeCH_4$ is larger as in $ArCH_4$ for high energy thresholds because of the already mentioned higher stopping power of xenon. For both counting gases, most of the events are detected in the overflow channel at 190 keV. In comparison with the event rate in the overflow channel the reduction of the events by enhancing the energy threshold is small. This causes the rather flat decrease. The presented efficiencies $\epsilon_{\mathrm{c,i}}$ of $ArCH_4$ and $XeCH_4$ were measured with one counter, respectively. The efficiencies were used in the calculation of the sensitivity for all measurements under the assumption that they are independent on the used counter.

[2]The daughter isotopes in the ^{222}Rn decay chain can get attached to the walls and the anode wire of the counter. This minimizes the solid angle which is available for the α emittance and thus its detection probability is reduced.

5.1.2 Decision Threshold

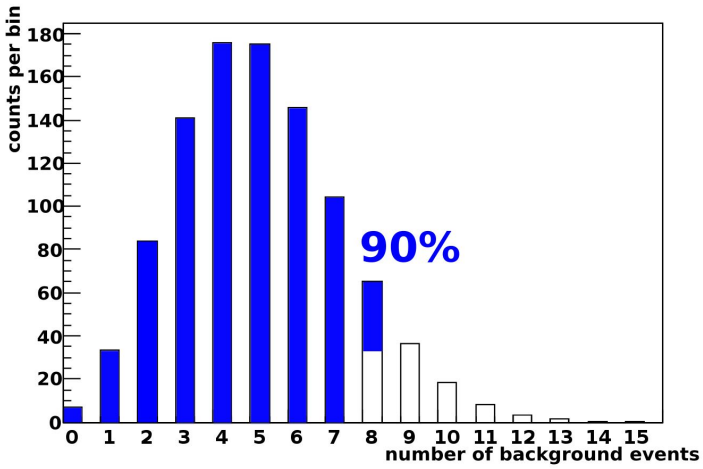

Figure 5.4: Poisson distribution with a demonstration of decision threshold's calculation. The proportion of the 90 % upper limit is not drawn to scale.

In this section we want to determine the decision threshold. The decision threshold describes a fixed value of the decision quantity by which, when exceeded by the result of an actual measurement of a measurand quantifying a physical effect, one decides that the physical effect is present [53]. In our case the decision quantity is a number of counts. If a measured number of counts exceeds the decision threshold we decide that, with a certain probability, the number does not arise from background but from the decay of ^{222}Rn of the sample. In the following we will determine the decision threshold $\tilde{\mathrm{N}}$ for different energy threshold of a background spectra. They are divided by the efficiency of the particular energy threshold and by the measurement time. This results in the sensitivity defined in Eq. 5.1.5. This sensitivity will have an error to consider the uncertainty arising from the correction of the efficiencies $\epsilon_{\mathrm{c,i}}^{\mathrm{Xe}}$ measured in $XeCH_4$. As described in section "Decrease of standard's activity" the efficiencies $\epsilon_{\mathrm{c,i}}^{\mathrm{Xe}}$ had to be corrected due to the decreased standard activity. We consider this uncertainty because we want to compare the sensitivites determined for $XeCH_4$ with the one for $ArCH_4$, for which no correction had to be applied. The common approach for the determination of the sensitivity is that one determines the decision threshold on the entire ratio

$$\tilde{\mathrm{S}}_i = \frac{\mathrm{N}_i}{\epsilon_{\mathrm{c},i} \cdot \mathrm{t}}\,, \tag{5.1.5}$$

whereby N_i is the number of counts above the energy threshold i. In this case the

sensitivity $\tilde{S}_i$ has no error. In the present case in which the efficiency in $XeCH_4$ is not precisely enough known the use of $\tilde{S}_i$ instead of S_i would not express correctly this uncertainty.Therefore we determine the decision threshold for the underlying distribution of N_i.

Many background measurement were done with diverse shielding and counting gas combinations that should be analysed in the following for the determination of the decision threshold.The energy spectra of these measurements were presented in chapter 4. The background spectra were recorded for a long measurement period t_{BG}. Thereby the detected number of events N_i^{best} above a certain energy threshold i can be considered as the best estimation of the background, for this measurement and the particular conditions like e.g. counting gas or applied shielding. Since regular measurement periods are much shorter as t_{BG} the number of events N_i^{best} were scaled to a period of $t = 10\,\text{days}$. This reflects a typical measurement period. The scaled number is referred to N_i^s. For this number N_i^s we want to determine the decision threshold. As N_i^s could be a small number its error is not Gaussian distributed but follows a Poisson distribution. Subsequent measurements yield most likely to a number of counts within this Poisson distribution $P(N_i^s)$. In a first step we distributed 10^3 events in a Poisson distribution with mean N_i^s. The shape of the Poisson distribution and hence the decision threshold depends strongly on the particular N_i^s in the range of small N_i^s. Therefor each of the events of $P(N_i^s)$ was in turn Poisson distributed.This should consider the uncertainty in in a measurement of a small number of events. The resulting Poisson distribution is referred to $P'(N_i^s)$.

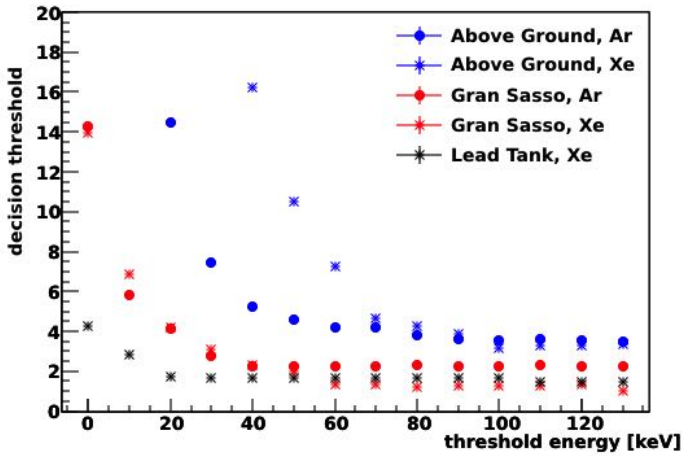

Figure 5.5: Decision thresholds for various counting gas/shielding combinations.

The decision threshold of P'(N_i^s) was determined. P'(N_i^s) was distributed around zero, as the background rate of the proportional counters is always subtracted in the evaluation of the sample's activity. We want to study the remaining background contribution. The decision threshold of P'(N_i^s) was set that exceeding results have a probability of less than 10 % to originate from background and not from the signal. The discrete Poisson distribution P'(N_i^s) was integrated to an upper limit of 90 % as indicated in Fig. 5.4. The binning of P'(N_i^s) was chosen that one integer corresponds to one bin. If the integral did not result in an integer number the contributing fraction of the particular bin was determined and added as decimal place. This means that a linear extrapolation between the two corresponding bins was used. Fig.5.5 shows the calculated decision thresholds for every energy threshold of one particular counter. The other counters show similar distributions. Indicated in different colors is the applied shielding using the same color mapping as in chapter 4. Thereby blue stands for "Above Ground", red for "Gran Sasso" and black for "Lead Tank". Dots are used to present background measurements in $ArCH_4$ and the crosses stand for measurements in $XeCH_4$. For increasing energy threshold i the decision threshold $\tilde{N}$ is decreasing since the background contribution becomes smaller for high energies. As the background spectra in chapter 4 already suggests the decision threshold is the highest for measurements above ground since the background event rate is the highest there.

5.2 Sensitivity results

In this section the results of the former two sections are combined for the calculation of the sensitivity S_i for different shielding/counting gas combinations of a particular counter. The decision threshold are divided by the measurement time and the efficiency of the corresponding energy threshold. The results can be seen in Fig. 5.6 - 5.7. The nomenclature is the same as previously introduced in chapter 4. The sensitivities are decreasing at low energies and become rather constant towards higher energies.

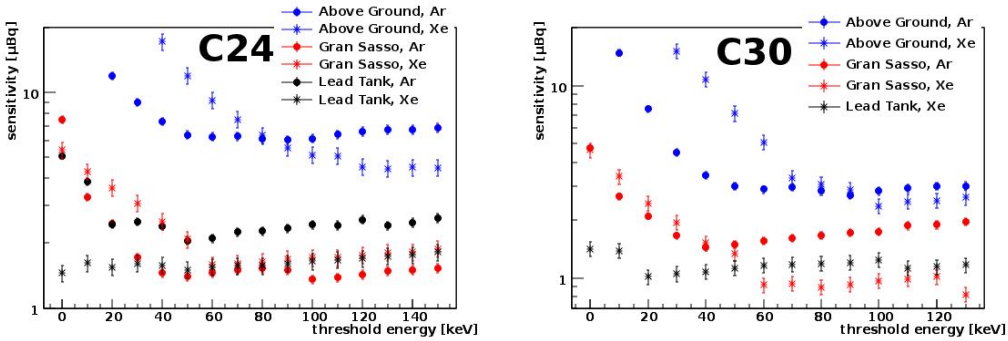

(a) *(b)*

Figure 5.6: ***(a)*** Sensitivity for measurements done with C24. ***(b)*** Sensitivity for measurements done with C30.

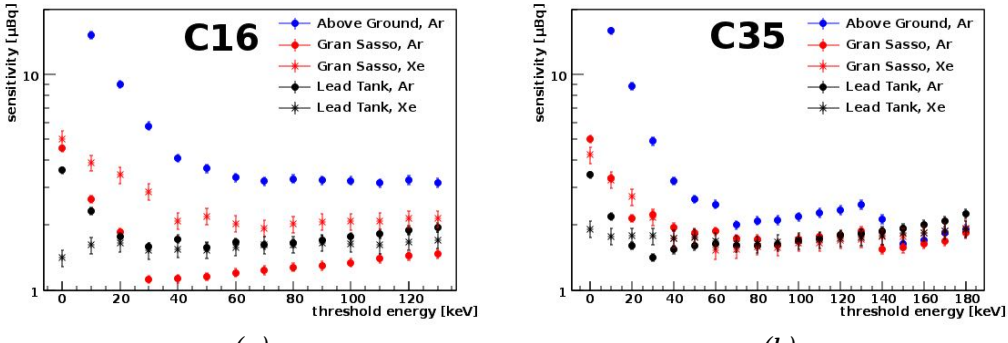

(a) *(b)*

Figure 5.7: ***(a)*** Sensitivity for measurements done with C16. ***(b)*** Sensitivity for measurements done with C35.

Fig. 5.8 shows a clearer picture of the sensitivities. Presented are the energy ranges in which the optimized sensitivity value of a particular counter is constant. There is no single energy threshold for which the sensitivity is maximized

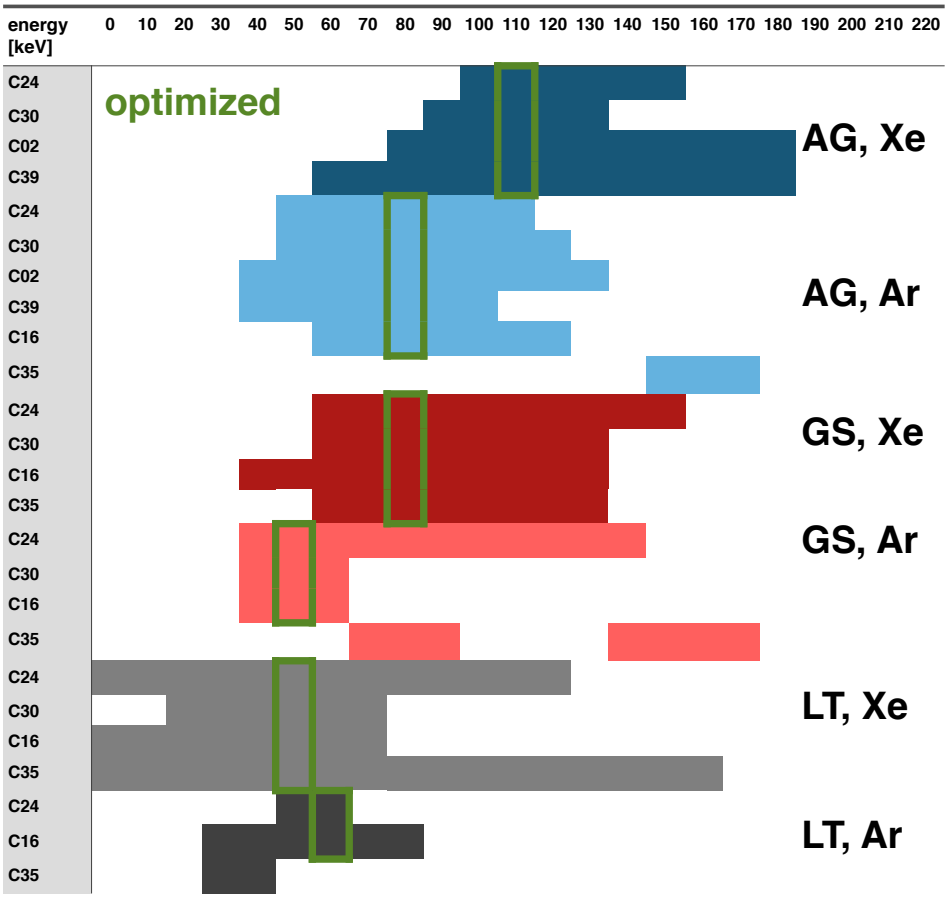

Figure 5.8: Indicated are the energy ranges with the lowest sensitivity for different counters and measurements.

but rather a broad energy range. The maximum error arising from the energy calibration is 10.7 %. The highest considered energy threshold is 110 keV in the following discussion. In this case the the error on the energy is 11.8 keV. In the chosen bin size of 10 keV an event could be at maximum misleadingly contribute to the next highest or lowest energy threshold. To account for this in the calculation for the sensitivity S'_i for a particular energy threshold i, the average of the sensitivities S_{i-1}, S_i and S_{i+1} was determined. For a particular class of counting gas/shielding the S'_i of different counters were averaged. These averaged sensitivity $\bar{S}'_i$ was calculated for three different thresholds:

- energy threshold at 50 keV that is used at the time of writing.
- energy threshold at 60 keV. At this energy threshold most of the maximized sensitivities are included.
- optimum energy threshold is set in the middle of the maximized sensitivity range to be stable against shifts in the energy determination due to the error in the energy calibration. The particular energy threshold is indicated in Fig. 5.8 in green if it differs from the threshold B. This study should verify if every counter and combination of counting gas/shielding requires another threshold.

	sensitivity [μBq]		
shielding/gas	50 keV	60 keV	optimum
AG, Ar	4.7 ± 0.4	4.5 ± 0.2	4.4 ± 0.2
AG, Xe	11.7 ± 1.1	-	5.5 ± 0.3
GS, Ar	1.5 ± 0.1	1.4 ± 0.1	1.5 ± 0.1
GS, Xe	1.7 ± 0.2	1.6 ± 0.2	1.6 ± 0.1
LT, Ar	1.8 ± 0.1	1.8 ± 0.1	1.8 ± 0.1
LT; Xe	1.5 ± 0.1	1.6 ± 0.1	1.6 ± 0.1

Table 5.1: Sensitivities, in units if [μBq] for different energy thresholds and for different combination of counting gas and shieldings. The nomenclature is the same as in chapter 4. The sensitivities were determined for an energy threshold at 50 keV, 60 keV and at an optimum threshold, that is most stable against the error arising from the energy calibration. Its particular value is indicated as a green box in Fig. 5.8.

The result of the averaged $\bar{S}'_i$ for the three mentioned energy thresholds are shown in Table 5.1. The column "50 keV" compares the average sensitivities for the diverse counting gas and shielding options at the energy threshold set at the moment of writing the thesis. In measurements above ground the sensitivity is worse by a factor of $\sim$2.5 in using $XeCH_4$ as counting gas and not $ArCH_4$. No clear preference of counting gas nor shielding is present for measurements in the underground laboratory at Gran Sasso by applying the recent energy threshold of 50 keV. The additional shield of the lead tank is not leading to a better sensitivity. The holds for an energy threshold of 60 keV. Excluded from this threshold are measurements above ground with $XeCH_4$ as they require a much higher threshold. The sensitivity of the optimal energy threshold are shown in the column "optimum". Only S_i were considered for which S_{i-1} and S_{i+1} are also included in the range of maximized sensitivity. For measurements above ground with $XeCH_4$ an energy threshold of 110 keV is suggested. In comparison to the

recent threshold at 50 keV the sensitivity can be improved by a factor of two. However the improved value of $XeCH_4$ is still worse as the best sensitivity in $ArCH_4$ independent on the particular chosen energy threshold. The reason is the generally higher background rate in $XeCH_4$ than in $ArCH_4$ at all energies. As the efficiency is independent on the counting gas this results in a worse sensitivity in $XeCH_4$. In the underground laboratory there is only a marginal difference between the background rates of different counting gases. This results in equal sensitivities for measurements done at Gran Sasso.

5.3 Conclusion

In chapter 5 we studied the performance of the two counting gases $ArCH_4$ and $XeCH_4$ in the detection of ^{222}Rn decays. This should lead to a further improvement of the precision of ^{222}Rn emanation measurements. The *sensitivity*

$$S_i = \frac{\tilde{N}_i}{\epsilon_{c,i} \cdot t}\,, \tag{5.3.1}$$

was introduced in order to compare measurements with different combinations of counting gas and shielding. In this study a scan over possible energy thresholds i is performed to optimize the detection sensitivity. The $\tilde{N}_i$ describes the *decision threshold*, a quantity defined to distinguish signal and background. The efficiency $\epsilon_{c,i}$ is the ratio of the measured activity above a certain energy threshold i relatively to the total activity. The time duration t describes the measurement period. The applied shieldings are discussed in chapter 4.

We observed no particular maximized sensitivity but rather a broad energy range of optimal sensitivity. We find that the differences in the efficiency $\epsilon_{c,i}$ are marginal for the two investigated counting gases. The considered background spectrum has a greater impact on the sensitivity.

The recent energy threshold at the time of writing is set at 50 keV independent on counting gas and shielding. For measurements above ground with $ArCH_4$ this energy threshold is confirmed. In contrast, an energy threshold between $100 - 130$ keV is recommended when using $XeCH_4$ as counting gas in measurements above ground. This leads to an increase in the sensitivity by a factor of 2 in comparison with the sensitivity at 50 keV. By traversing the small active volume of the proportional counter, particles can depose more of their energy in xenon than in argon. This leads to a shift towards higher energies of the background spectrum in $XeCH_4$ compared with the one of $ArCH_4$. This effect is most dominant above ground as the main background contribution arises from high energetic muons. Therefor the energy threshold needs to be higher for measurements with $XeCH_4$ in comparison to measurements with $ArCH_4$.

For measurements performed in the underground laboratory the high energetic background component is sufficiently stopped by the rocks surrounding the laboratory.The remaining background events are rather low energetic and the shift

of the $XeCH_4$ spectrum towards high energies is negligible. Hence the threshold for $XeCH_4$ does not need to be enhanced for an improvement of the sensitivity. An energy threshold of 50 keV is optimal, independent on the counting gas. The sensitivities are the same for both counting gases. Furthermore there is no difference in using lead bricks or a enhanced shielding with the lead tank.

The maximized sensitivity at the optimal energy threshold for the various counting gas/shielding combinations are given in Table 5.2. The sensitivities of the measurements in the underground laboratory were combined as they do not differ significantly. The sensitivity is enhanced by a factor of ~ 3 and ~ 3.4 in comparison with measurements above ground in $ArCH_4$ and $XeCH_4$, respectively. Above ground the counting gas $ArCH_4$ is preferred.

shielding/gas	threshold [keV]	sensitivity [μBq]	efficiency [%]
AG, Ar	50	4.7 ± 0.4	1.50 ± 0.07
AG, Xe	110	5.5 ± 0.3	1.34 ± 0.12
GS, Ar GS, Xe LT, Ar LT, Xe	50	1.6 ± 0.1	1.50 ± 0.07

Table 5.2: Final sensitivities and optimal energy threshold for the used combination of counting gas and shieldings whereby the nomenclature is the same as in chapter 4.

Summary

The focus of this Master thesis is placed on the detection of the radioactive ^{222}Rn with miniaturized proportional counters. The noble gas ^{222}Rn is one of the most challenging intrinsic background sources for experiments searching for rare events. It is permanently emanating from almost all materials and consequently also from the detector components. This motivates material screening and selection of only the most radio-pure components before detector construction.

In the context of the dark matter search experiment XENON1T an extensive measurement campaign was performed in order to determine the ^{222}Rn emanation rates of the detector materials that will be in contact with the target material xenon. The results of these emanation measurements for the individual components can be found in chapter 2. By summing up the individual rates we estimate an overall emanation rate of $A_{ind.} = (30 \pm 1)\,\mathrm{mBq}$ for the XENON1T detector. This corresponds to roughly ~ 15000 ^{222}Rn atoms in the entire system. The measured overall emanation rate exceeds the XENON1T goal of 3 mBq in ~ 3.3 tons of liquid xenon. However, it is not clear if both rates can be directly compared as they imply different conditions. The measurements were performed with carrier gases different from xenon and at other thermal conditions as they will be present in the liquid xenon at a temperature of $\sim 180\,\mathrm{K}$. The knowledge we gained during the measurement campaign will be also valuable in the material selection of the future project XENONnT.

While the first part of this thesis considers a direct application of the ^{222}Rn detection with miniaturized proportional counters, the second part aims at improving this detection method. We compared the two counting gases $ArCH_4$ and $XeCH_4$ regarding their performance in the detection of ^{222}Rn decays. This makes an energy calibration necessary. Counters filled with $XeCH_4$ were calibrated by the already existing method of using excited cerium that generates energy depositions up to $\sim 39\,\mathrm{keV}$ in the counting gas. For counters filled with $ArCH_4$ a

^{55}Fe x-ray source is used inducing a single peak at $\sim 6\,\mathrm{keV}$ that can be used for calibration. In order to calibrate over a larger energy scale and testing the energy scale's linearity a new calibration method was successfully developed for $ArCH_4$. It bases on admixing a small amount of xenon atoms that serve as a target for the cerium calibration source. This new method allows a calibration in the same energy range as in $XeCH_4$ and an improved comparison of measurements done with the two investigated counting gases. We think that the peak fitting of the calibration spectrum could be further improved by a better background understanding which could be provided by a Monte Carlo study.

In chapter 4 we applied the energy calibration for the comparison of background spectra measured with $ArCH_4$ and $XeCH_4$. The background spectra were recorded over a combined total data taking time of roughly 3.5 years, with 4 proportional counters and by applying 3 different shieldings. The first option is a set-up above ground, in a laboratory at MPIK using lead bricks. The second and third shielding options are both in an underground laboratory at Gran Sasso. Whereas the second option uses an equal set-up as above ground, the third shielding is more sophisticated. It consists of a lead tank with 4π coverage, enclosed in a stainless steel container and permanently flushed with boil-off nitrogen. The total background rate is reduced by $\sim$2 orders of magnitude by comparing measurements above ground and underground. In the underground laboratory no significant difference of the total background rates was observed in measurements using $ArCH_4$ inside or outside the lead tank. A comparable total background rate outside the lead tank was identified for $XeCH_4$. In contrast, the total background rate inside the tank is reduced by a factor of $\sim$7 for the same counting gas. This decrease of the background rate is not understood,yet.

In the last chapter the background measurements were combined with the efficiency of the ^{222}Rn detection in order to determine the optimized sensitivity at a certain energy threshold. In measurements above ground, using $ArCH_4$ we identified an optimized sensitivity at an energy threshold of 50 keV. In contrast, for measurements using $XeCH_4$ an energy threshold at 110 keV is suggested. However, the optimized sensitivity in $XeCH_4$ is still worse than the one using $ArCH_4$ above ground, which favors $ArCH_4$ as counting gas in measurements there. For measurements performed at Gran Sasso, either inside or outside the lead tank, the the optimized energy threshold is identified at 50 keV, independent on the counting gas. The sensitivity is enhanced by a factor of ~ 3 and ~ 3.4 in com-

parison with measurements above ground in $ArCH_4$ and $XeCH_4$, respectively. This means that, among the studied shielding options, measurements performed in the underground laboratory at Gran Sasso provide the maximal sensitivity for ^{222}Rn detection.

Appendix A

Formula of time evolution

Calculated time evolution of an activity A_{sample}. Included is the rising phase and the radioactive decay. Thereby only the α-decays in the decay chain of Eq.5.1.3 generate the signal. The β-particles are neglected.

$$A(t) = A_0\, e^{-\lambda_a \cdot t} + A_0 \left(\frac{\lambda_b}{\lambda_b - \lambda_a}\right)(e^{-\lambda_a\, t} - e^{-\lambda_b\, t}) + A_0\, \lambda_b\, \lambda_c\, \lambda_d\, \lambda_e\, Y\,, \quad \text{(A.0.1)}$$

whereby

$$\begin{aligned} Y = &\frac{e^{-\lambda_a\, t}}{(\lambda_b - \lambda_a)(\lambda_c - \lambda_a)(\lambda_d - \lambda_a)(\lambda_e - \lambda_a)} + \frac{e^{-\lambda_b\, t}}{(\lambda_a - \lambda_b)(\lambda_c - \lambda_b)(\lambda_d - \lambda_b)(\lambda_e - \lambda_b)} \\ &+ \frac{e^{-\lambda_c\, t}}{(\lambda_a - \lambda_c)(\lambda_b - \lambda_c)(\lambda_d - \lambda_c)(\lambda_e - \lambda_c)} + \frac{e^{-\lambda_d\, t}}{(\lambda_a - \lambda_d)(\lambda_b - \lambda_d)(\lambda_c - \lambda_d)(\lambda_e - \lambda_d)} \\ &+ \frac{e^{-\lambda_e\, t}}{(\lambda_a - \lambda_e)(\lambda_b - \lambda_e)(\lambda_c - \lambda_e)(\lambda_d - \lambda_e)} \end{aligned}$$

and λ_a-λ_e define the decay constants from ^{222}Rn to ^{214}Pb within the ^{238}U decay chain. The formula is taken from [19]

Bibliography

[1] R. Abbasi et al. (The IceCube Collaboration), *Multiyear search for dark matter annihilations in the sun with the amanda-ii and icecube detectors*, Phys. Rev. D85 (2012).

[2] R. Agnese et al., *Search for Low-Mass WIMPs with SuperCDMS*, arXiv:1402.7137 (2014).

[3] D. S. Akerib et al., *First results from the LUX dark matter experiment at the Sanford Underground Research Facility*, arXiv:1310.8214 (2014).

[4] A. J. Anderson and SuperCDMS Collaboration *Phonon-Based Position Determination in SuperCDMS iZIP Detectors*, J.Low Temp.Phys. 176 (2014) 959-965, arXiv:1405.4215 (2014).

[5] E. Aprile et al. , *Performance of a cryogenic system prototype for the* XENON1T *Detector* arXiv:1208.2001v2 (2012).

[6] E. Aprile et al. (XENON100 Collaboration), XENON1T *at LNGS Technical Design Report, October 2012*.

[7] E. Aprile et al. (XENON100 Collaboration) *The Xenon100 Dark Matter Experiment*, arXiv:1107.2155 (2012).

[8] E. Aprile et al. (XENON100 Collaboration) *Study of the electromagnetic background in the* XENON100 *experiment*, Phys. Rev. D, 83 (2013).

[9] E. Aprile et al. (XENON100 Collaboration) *Analysis of the Xenon100 Dark Matter Search Data*, arXiv:1207.3458v3 (2013).

[10] E. Aprile et al., *The XENON1T Dark Matter Search Experiment*, arXiv:1206.6288v1 (2014).

[11] W. B. Atwood et al, *The Large Area Telescope on the Fermi Gamma-ray Space Telescope Mission*, Astrophys.J., 697:1071-1102 (2009).

[12] H. Baer and X. Tata, *Dark matter and the LHC*, arXiv:0805.1905 (2008).

[13] V. Barger, W.-Y. Keung, D. Marfatia, and G. Shaughnessy, *PAMELA and dark matter*, Phys.Lett., B672:141-146 (2009).

[14] J. J. Beatty *Review on cosmic rays* Particle Data Group (2013).

[15] J. Beringer et al. *Review on particle detectors for non-accelerator physics*, Particle Data Group (2012).

[16] G. Bertone, *Particle Dark Matter. Observations, Models and Searches*, Cambridge University Press (2010).

[17] H. Bichsel et al. *Review on passage of particles through matter*, Particle Data Group (2005).

[18] J. R. Bond, G. Efstathiou, and J. Silk, *Massive Neutrinos and the Large-Scale Structure of the Universe*, Phys. Rev. Lett. 45 (1980).

[19] S. Brünner, *Study of radon adsorption on activated carbon for a purification system in* XENON1T, Dipl. Thesis, Universität Graz (2013).

[20] S. Cecchini *Atmospheric muons: experimental aspects*, arXiv:1208.1171v1 (2012).

[21] E. Fernandez-Martinez and R. Mahbubani *The Gran Sasso muon puzzle*, arXiv:1204.5180 (2012).

[22] N. Ferrari *Laboratori Nazionali del Gran Sasso and the Ilias Initiative*, Laboratoire Souterrain de Modane (2012).

[23] P. J. Fox, R. Harnik, J. Kopp, and Y. Tsai, *Missing Energy Signatures of Dark Matter at the LHC*, Phys.Rev., D85:056011 (2012).

[24] G. Heusser, *Low-Radioactivity Background Techniques*, Max-Planck-Institut für Kernphysik, Heidelberg (1995).

[25] H. Hirayama, *Lecture Note on Photon Interactions and Cross Sections*, KEK, High Energy Accelerator Research Organization Ibaraki, Japan (2000).

[26] D. Hooper and S. Profumo, *Dark matter and collider phenomenology of universal extra dimensions*, Phys.Rept., 453:29-115 (2007).

[27] R. Jenkins, R. W. Gould, D. Gedcke, *Quantitative X-Ray Spectrometry, Second Edition*, Marcel Dekker Company (1995).

[28] G. Jungman, M. Kamionkowski, and K. Griest, *Supersymmetric dark matter*, Phys.Rept., 267:195-373 (1996).

[29] W. R. Leo *Techniques for Nuclear and Particle Physics Experiments*, Springer-Verlag (1978).

[30] J. Lewin and P. Smith, *Review of mathematics, numerical factors, and corrections for dark matter experiments based on elastic nuclear recoil*, Astropart. Phys. 6 87 (1996).

[31] S. Lindemann, *Reinigung und Nachweis von Edelgasen mit miniturisierten Proportionalzählren*, Dipl. Thesis, Universität Heidelberg (2009).

[32] S. Lindemann, *Intrinsic ^{85}Kr and ^{222}Rn Background in the Xenon Dark Matter Search*, Dissertation, University of Heidelberg (2013).

[33] V. A. Kudryavtsev, L. Pandola, and V. Tomasello *Neutron- and muon-induced background in underground physics experiments*, Department of Physics and Astronomy, University of Sheffield, Sheffield, United Kingdom and INFN, Laboratori Nazionali del Gran Sasso, Assergi, Italy (2005).

[34] T. Marrodan Undagoitia, *Revealing the nature of dark matter with XENON*, Habilitation Summary (2014).

[35] B. R. Martin and G. Shaw, *Particle Physics, third edition*, John Wiley and Sons Inc. (2008).

[36] F. V. Massoli, *The XENON1T experiment: Monte Carlo background estimation and sensitivity curves study*, Ph.D. thesis, Universita di Bologna, Italy (2015).

[37] H. Nikjoo *Interaction of radiation with matter*, Taylor and Francis Group, US (2012).

[38] Planck Collaboration, *Planck 2013 results. I. Overview of products and scientific results*, arXiv:1303.5062 (2013).

[39] W. Rau, *Low-Level Radonmessungen für das Sonnenneutrinoexperiment Borexino*, Ph.D. Thesis, Universität Heidelberg (1999).

[40] B. Richard, B. Firestone and S. S. Virginia, *Table of Isotop es Eighth Edition*, John Wiley and Sons, Inc. (1996).

[41] V. C. Rubin, N. Thonnard, and J. Ford, *Extended rotation curves of high-luminosity spiral galaxies*, Astrophys. J 225 L107 (1978).

[42] SAES Getters S.p.A, webpage: http://www.saesgetters.com

[43] F. Sauli, *gaseous detector fundaments*, Talk (2011).

[44] H. Simgen *Hochempfindlicher Nachweis radioaktiver Edelgasnuklide und natürlicher Radionuklide aus der Uran-Zerfallsreihe*, Dissertation, University of Heidelberg (2003).

[45] H. Simgen, G. Heusser and G. Zuzel *Highly sensitive measurements of radioactive noble gas nuclides in the Borexino solar neutrino experiment*, Appl. Radiat. Isot. 61,213 (2004).

[46] H. Simgen et al. *Detection of ^{133}Xe from the Fukushima nuclear power plant in the upper troposphere above Germany*, arXiv:1309.1618 (2013).

[47] I. B. Smirnov, Nucl. Instr. and Meth. A 554(2005)474, Talk (2011).

[48] M. C. Smith et al., RAVE Collaboration, *The RAVE survey: constraining the local Galactic escape speed* MNRAS 379 (2007) , arXiv:astro-ph/0611671v2.

[49] A. Sonnenschein *Measurement of Ar-39 in Argon*, Fermilab (2012).

[50] E. Storm and H. I. Israel, *Photon cross section from 1 keV to 100 Mev for elements Z = 1 to Z = 100*, Los Alamos Scientific Laboratory, University of California Los Alamos, New Mexico (1970).

[51] A. Urban, *Analyse von Proportionalzählrohrimpulsen zum Nachweis von solaren Neutrinos*, Ph.D. Thesis, Universität München (1989).

[52] M. Weber, *Gentle Neutron Signals and Noble Background in the XENON100 Dark Matter Search Experiment*, PhD Thesis, Universität Heidelberg (2013).

[53] K. Weise, *Determination of the detection limit and the decision threshold for ionizing radiation measurements: fundamentals and particular applications*, Fachverband für Strahlenschutz .

[54] L. M. Widrow, B. Pym, and J. Dubinski, *Dynamical Blueprints for Galaxies*, Astrophys. J. 679 1239, arXiv:0801.3414 (2008).

[55] K. Zuber *Neutrino Physics*, Institute of Physics, London (2004).

[56] G. Zuzel, H. Simgen *Applied radiation and Isotope: high sensitivity radon emanation measurements*, published by Elsevier Ltd. (2009).

[57] F. Zwicky, *Die Rotverschiebung von extragalaktischen Nebeln*, Helvetica Physica Acta 6 110 (1933).

[58] *private communication with G. Heusser and W. Hampel.*

[59] *private communication with H. Simgen.*

[60] *internal communication with XENON Collaboration.*

[61] webpage: http://ie.lbl.gov, *The Isotopes Project Home Page*, Lawrence Berkeley National Laboratory.

[62] webpage: http://ie.lbl.gov, *X-Ray Data Booklet*, Lawrence Berkeley National Laboratory.

[63] webpage: *http://rimg.geoscienceworld.org*

Danksagung

Ich danke Prof. Manfred Lindner, der mir die Möglichkeit gegeben im XENON Experiment an der Front der Forschung mitzuwirken und für den Anstoß mich auch an Laborarbeiten zu trauen, was sich auf jeden Fall gelohnt hat. Außerdem danke ich Prof. Norbert Herrmann, der sich bereit erklärt hat, die Zweitbegutachtung der Arbeit zu übernehmen.

Des Weiteren bedanke ich mich bei der "Radon-Crew", allen voran Hardy, für das geduldige Beantworten meiner vielen Fragen, das Zutrauen auch von größeren Aufgaben und die entspannte Arbeitsatmosphäre. Sebastian danke ich für seine guten Ratschläge im letzten Jahr und das gründliche und hilfreiche Korrekturlesen dieser Arbeit. Nicht genug danken kann ich wohl Stefan für seine freundschaftliche Unterstützung in vielen Situationen und für die Einführung in die österreichische Sprach, Lied -und Filmkultur. Jonas danke ich für die Einweihung in die Kunst des Zählrohrfüllens und die Hilfe bei den alltäglichen Laborarbeiten.

Ich bedanke mich bei der gesamten XENON Gruppe, für ihre ansteckende Begeisterung und Hilfe in vielen Fragen. Dank gilt des weiteren allen Kollegen und Freunden am Institut, die mir in irgendeiner Weise geholfen, besonders Alex, meinem lieben Schreibtischnachbarn.

Ich danke allen Menschen, die mir zeigen, dass es sich lohnt, seinen Weg zu gehen und meinen Freunden, die mir dafür den nötigen Mut geben. Dabei denke ich auch an Tanja und Meike, meinen wichtigsten Begleiterinnen durch das Studium, denen ich fürs Zusammenhalten danke. Außerdem bedanke ich mich bei Julia, für ihre tatkräftige Unterstützung in allen Lebenslagen. Mynyna danke ich im Grunde dafür, dass sie so ist, wie sie ist.

Meinen beiden geliebten Schwestern und Eltern danke ich für den bedingungslosen Rückhalt und das Mitfühlen, bei allem was ich erlebe.

Erklärung

Ich versichere, dass ich diese Arbeit selbständig verfasst und keine anderen als die angegebenen Quellen und Hilfsmittel benutzt habe.

Heidelberg, den 01.05.2015

Natascha Rupp